Optimization of Tungsten Electropolishing for Enhanced Anodic Nanostructured WO_3 Growth in Solar Water Splitting

Jorge Fernandes
Mestrado em Engenharia Física
Departamento de Física e Astronomia
2023

Supervisor
Prof. Dra. Arlete Apolinário, Doutorada de Nível Inicial, Faculdade de Ciências

Co-supervisor
Prof. Dr. João Araújo, Professor Associado, Faculdade de Ciências


U.PORTO
FACULDADE DE CIÊNCIAS
UNIVERSIDADE DO PORTO

" I will keep making planes until one of them flies. "

Brian Baumgartner as Kevin Malone in *The Office*.

Acknowledgements

First and foremost, I want to express my heartfelt appreciation to everyone who helped me with my thesis. To everyone without whom this would not have been possible. I am deeply thankful for all the great support and advice I was showered with.

I would like to sincerely thank my supervisor, Doctor Arlete Apolinário for everything she has done for me. I am truly grateful for the opportunity to work in such a unique and interesting project and for all that I learned from her in this journey.

I would like to thank my co-supervisor, Professor João Pedro Araújo, for the chance of being a member of such a remarkable and distinguished research group and for all the critical advice.

I would also like to thank all the people who worked with me in the laboratory. Every minor and urgent issue was solved thanks to them.

Aos meus amigos que me acompanharam ao longo desta etapa universitária, um enorme obrigado por todo o apoio e memórias proporcionadas. Sem vocês nada disto seria possível. Amizades que levo para a vida.

Por último, agradecer à minha família. Aos meus pais, Jorge e Cristina, à minha irmã, Ana, e aos meus avós, Teresa e António, que sempre me acompanharam e apoiaram, pilares da minha vida. Aos meus restantes familiares, um grande obrigado por tudo o que já fizeram por mim.

Institutions Involved

Funding

This master thesis was supported by FCT—Fundação para a Ciência e a Tecnologia by projects NORTE-01-0145-FEDER-000076 (H2INNOVATE) and project H2FlexiPECs's (ref. 2022.07332.PTDC). The author acknowledges the MSCA-RISE-734801-MAGNAMED project, UIDB/04968/2020, UIDB/04968/2021, LA/P/0095/2020. Arlete Apolinário acknowledges FCT - Fundação para a Ciência e a Tecnologia, contract DL57/2016 (ref. SFRH / BPD / 82010/2011) and the H2FlexiPEC project (ref. 2022.07332.PTDC).

UNIVERSIDADE DO PORTO

Abstract

Faculdade de Ciências da Universidade do Porto
Departamento de Física e Astronomia

MSc. Engineering Physics

Optimization of Tungsten Electropolishing for Enhanced Anodic Nanostructured WO_3 Growth in Solar Water Splitting

by Jorge FERNANDES

Recent studies have suggested that tungsten trioxide (WO_3) is a suitable semiconductor for photoelectrochemical (PEC) applications due to its advantageous characteristics such as a suitable band gap, chemical stability, and high resistance to photocorrosion. Depending on the fabrication techniques used, various WO_3 nanostructures can be synthesized. Electrochemical anodization is a cost-effective and simple technique that can be used to create highly organized nanoporous (NPs) and nanotubes (NTs) oxides, which have been widely reported for titanium dioxide (TiO_2) and hematite (α-Fe_2O_3). Prior to the implementation of this synthesis method, the metallic surfaces may reveal unsuitable profiles that hinder the growth of NTs. Thus, electropolishing (EP) can be used as a surface pre-treatment to obtain smooth metallic surfaces that improve the subsequent NT growth quality in terms of growth rate and NTs organization. In order to be suitable for PEC applications, the initially obtained anodic nanoporous structures must undergo thermal annealing, allowing the amorphous oxide to transition into a crystalline state (semiconductor).

This thesis investigated the effect of tungsten (W) EP and thermal annealing on the performance of nanostructured WO_3 photoanodes fabricated by electrochemical anodization, with the aim of creating a suitable semiconductor for solar water splitting. To do so, a comprehensive research study was done regarding the ideal tungsten (W) EP conditions to be implemented in the W surface prior to the anodization process, since the application of such surface treatment to W for producing self-ordered WO_3 NTs has limited scientific coverage. Additionally, the effects of thermal annealing parameters on PEC performance were assessed as well.

The EP optimization study enabled the determination of optimum parameters for different EP variables. Through an examination of the W polarization curve, it was observed that the rate of electrolyte rotation influences the formation of the EP viscous layer, which influences the EP effectiveness. The EP outcome experienced substantial influence from variations in electrolyte concentration. Higher concentrations led to continuous etching, causing damage to the W surface. This prompted the selection of an aqueous electrolyte with a concentration of 0.125M NaOH. In-depth topographical analysis employing Atomic Force Microscopy (AFM) in conjunction with Scanning Electron Microscopy (SEM) morphological analysis unveiled that the W surface roughness exhibited an exponential decrease as the EP time extended. This transitioned from dimple-patterned surfaces for shorter EP times to smoother surfaces for longer durations.

The impact of EP conditions on the W anodization process was evaluated. The ideal EP parameters had a significant effect on the growth of WO_3 NTs. Using SEM images for morphological characterization, it was found out that the surface pre-treatment led to a decrease in pore competition, which enabled a more prominent vertical growth of the NTs. The EP caused a considerable influence on the NTs porosity, expressed in the 179% mean porosity increase compared to the anodization performed in the W sample without EP, leading to an improvement in the surface area. The combination of the topography and morphology images enabled the analysis of the anodized W EP samples pre-treated with an EP with a potential of either 10V or 15V during 2, 10 or 60 minutes. The results revealed that dimple-patterned W surfaces enhanced the fabrication of highly ordered WO_3 NT arrays, with the EP under 10V, 2 minutes producing a nanoporous layer with a porosity value of 46.2% and 398 nm of NT length. On the other hand, W samples exhibiting high roughness with non-uniform surface profiles or low roughness values with a high smoothing effect revealed to grow the oxide as a dense film after producing a thin NT layer in the anodization nucleation stage.

Further research was done on the influence of annealing parameters in the PEC performance. The structural characterization by X-Ray Diffraction (XRD) of the annealed WO_3 revealed that the most effective photoperformance was achieved when the thermal treatment was carried out at 500ºC with a heating rate of 2°C per minute, while also confirming the presence of typical crystallographic planes related to the monoclinic phase of WO_3. This process also formed an oxide layer beneath the nanoporous layer that had been created through anodization.

Using the previously optimized EP and annealing parameters, PEC characterization by photocurrent-voltage characteristic curves was used to evaluate the effect of these treatments on the photoperformance of nanostructured WO_3. Applying EP to the W surface revealed to impact the photocurrent density by increasing it by 5%, registering a value of 143 $\mu A.cm^{-2}$. The onset potential indicated similar potential requirements to start the water splitting reaction for both W surface profiles.

UNIVERSIDADE DO PORTO

Resumo

Faculdade de Ciências da Universidade do Porto
Departamento de Física e Astronomia

Mestrado em Engenharia Física

Otimização do Eletropolimento de Tungsténio para Aprimoramento do Crescimento de WO_3 Anódico Nanoestruturado em Separação Solar da Água

por Jorge FERNANDES

Estudos recentes sugerem que o trióxido de tungsténio (WO_3) é um semicondutor adequado para aplicações fotoeletroquímicas (PEC) devido às suas vantajosas características como estreita largura de banda, estabilidade química, e alta resistência à fotocorrosão. Dependendo das técnicas de fabricação usadas, várias nanoestruturas de WO_3 podem ser sintetisadas. Anodização eletroquímica é uma técnica simples e de baixo custo que pode ser usada para criar nanoporos (NPs)/ nanotubos (NTs) de óxidos com elevada organização, sendo a sua utilização vastamente reportada para dióxido de titânio (TiO_2) e hematite (α-Fe_2O_3). Antes da implementação deste método de síntese, as superfícies metálicas podem revelar perfis inapropriados que não auxiliam o crescimento de NTs. Assim, eletropolimento (EP) pode ser utilizado como um tratamento de superfície para obter superfícies metálicas lisas e suaves com o objetivo de melhorar a qualidade do consequente crescimento de NTs. Para poderem ser utilizadas em aplicações PEC, as estruturas nanoporosas desenvolvidas por anodização necessitam de ser submetidas a um recozimento térmico para transitar de um óxido amorfo para um estado cristalino (semicondutor).

Esta tese investigou o efeito do eletropolimento de tungsténio (W) e do recozimento térmico no desempenho de fotoânodos nanoestruturados de WO_3 fabricados por anodização eletroquímica, com o objetivo de criar um semicondutor adequado para a separação solar de água. Para tal, foi realizada uma investigação compreensiva relacionada com as condições ideais para a aplicação do EP na superfície de W antes da implementação da anodização, uma vez que a aplicação deste tratamento de superfície a W para produzir

NTs de WO_3 auto-organizados tem limitada cobertura científica. Adicionalmente, os efeitos dos parâmetros do recozimento térmico no desempenho PEC foram avaliados.

O estudo de otimização de EP permitiu a determinação the parâmetros ideais para diferentes variáveis do processo. Analizando a curva de polarização de W, descobriu-se que a velocidade de rotação do eletrólito tem um efeito na formação da camada viscosa do EP. Para velocidades elevadas, esta camada foi removida em excesso, resultando no valor ideal obtido de 0 rotações por minuto (rpm). O resultado do EP foi significativamente impactado por mundanças na concentração do eletrólito. Valores altos resultaram em danos na superfície de W através de contínuo ataque químico na mesma. Isto levou à escolha do eletrólito aquoso com 0.125M NaOH. A combinação de análise topográfica usando Atomic Force Microscopy (AFM) e de análise morfológica com Scanning Electron Microscopy (SEM) revelou que a rugosidade da superfície de W diminuiu exponencialmente com o aumento do tempo de EP. O perfil da superfície de W transitou de superfícies onduladas e uniformes para tempos reduzidos para superfícies lisas para valores longos.

O impacto das condições de EP obtidas na andodização de W foi avaliado. Os parâmetros de EP ideais tiveram um efeito significativo no crescimento de NTs de WO_3. Através de análise morfológica usaando imagens de SEM, descobriu-se que a introdução do prétratamento de superfície levou a uma redução na competição entre poros, que por sua vez permitiu um crescimento vertical de NTs mais proeminente. O EP teve uma influência considerável na porosidade dos NTs, expressa no aumento de 179% de porosidade média comparado com a anodização realizada na amostra de W sem EP, o que levou a um aumento da área de superfície. A combinação da análise topográfica e morfológica permitiu descobrir que superfícies que revelaram ter padrões de ondulação permitiram a fabricação de redes de NTs de WO_3 com elevada organização, com o EP sob 10V, 2 minutos produzindo uma camada de NTs com 46.2% de porosidade e 398 nm de comprimento de NT. Por outro lado, amostras de W que revelaram elevada rugosidade com perfis não-uniformes ou baixos valores de rugosidade com superfícies lisas permitiram o crescimento do óxido sob a forma de um filme denso após a formação de uma camada fina de NTs na fase de nucleação da anodização.

A influência dos parâmetros de annealing no desempenho PEC foi investigada. A caracterização estrutural através de X-Ray Diffraction (XRD) das amostras de WO_3 submetidas a recozimento térmico revelou que o melhor fotodesempenho era alcançado com um tratamento térmico a 500ºC e com uma rampa de aquecimento de 2ºC por minuto.

Esta caracterização também confirmou a presença de planos cristalográficos típicos da fase monoclínica de WO_3. O tratamento considerado revelou ainda a formação de uma barreira de óxido abaixo da camada nanoporosa que foi criada através da anodização.

Usando os parâmetros de recozimento térmico e de EP anteriormente otimizados, uma caracterização PEC através de curvas características de fotocorrrente-potencial foi utilizada para avaliar o efeito destes tratamentos no fotodesempenho de WO_3 nanoestruturado. A aplicação de EP em W revelou provocar um aumento de 5% na densidade de fotocorrente, registando um valor de 143 μA.cm^{-2}. O potencial de ativação indicou requerimentos de potencial para iniciar a reação de separação solar da água similares para ambos os perfis de superfície de W.

Contents

List of Figures

List of Tables

Chapter 1

Introduction

1.1 Energy: Global Emergency

Current generations are faced with an unprecedented challenge. To reduce reliance on fossil fuels, drastic modifications must be made at the industrial level. To ensure a better world for future generations, urgent and decisive action must be taken.

The world population has grown from 1.6 billion people in 1990 to 7.2 billion in 2016 [1]. This rapid expansion has caused an unsustainable increase in global energy consumption, with fossil fuels accounting for 79.6% of energy production in 2002 [2]. This has led to a sharp increase in CO_2 and other greenhouse gas levels. Despite this, the energy sector is still heavily reliant on fossil fuels (around 80%) [3], which are the main cause of global warming [4]. It is therefore essential to reduce the use of fossil fuels in our daily lives. Predictions suggest that electricity needs will double by 2050, making a major energy revolution unavoidable [3].

Nonrenewable energy sources, such as fossil fuels, are finite and will eventually be depleted. There is no definite timeline for when they will be completely replaced. The main issues that need to be addressed are cost effectiveness, environmental friendliness, and accessibility of energy for all. Renewable energies have the potential to reduce carbon emissions by 90% in the electricity sector by 2050 [5], so it is essential to focus on researching and developing eco-friendly energy solutions.

The Sun is an inexhaustible source of energy, capable of supplying humanity's yearly total energy needs in just one hour ($4.6 \cdot 10^{20} J$) [4]. However, only a fraction of the total solar radiation emitted from the Sun reaches the Earth's surface (above 100000 TW) due to reflection and absorption [6, 7]. This has led to increased interest in solar conversion

systems, as investors have recognized them as a potential solution to the global energy crisis. Over the past 30 years, solar technologies have seen an annual growth of 30%, largely due to the reduction in installation costs [8]. As such, solar energy is one of the most promising sources of energy currently studied, with the potential to meet the world's energy needs for current and future generations.

1.2 Photoelectrochemical Cells for Solar Water Splitting as Harvesting Solution

Photovoltaic systems (PV) have seen rapid growth in recent years as one of the primary sources of energy production from solar energy. These systems are composed of components that convert light into electricity, with the main component being a solar cell. After extensive research into PV systems, solar cells that can collect solar energy and produce green hydrogen have been developed. Sunlight-generated hydrogen is an attractive energy source, as it is transportable, storable, and can be converted into electricity for mobile and stationary applications [9].

Photoelectrochemcial cells (PECs) enable the transformation of photon energy into chemical energy. This is accomplished by the splitting of water into hydrogen and oxygen. The PEC system is typically composed of a photoelectrode (an n-type or p-type semiconductor, also known as the working electrode) and a counter-electrode (such as a metallic piece of platinum), both submerged in an electrolyte that contains specific redox couples that facilitate chemical reactions (see Figure 1.1).

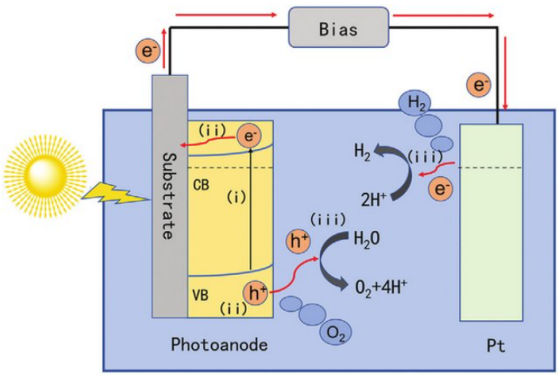

FIGURE 1.1: Schematic of a PEC cell with a n-type photoanode and reactions involved in water splitting in an aqueous electrolyte at pH = 0 [10].

The PEC water splitting process can be broken down into three distinct stages (see Figure 1.1): (i) light absorption in the semiconductor generates electron-hole pairs; (ii) electrons are transported to the counter-electrode (CE) via an external circuit, while holes diffuse to the semiconductor/electrolyte interface; (iii) charge carriers participate in the hydrogen evolution reaction (HER) and oxygen evolution reaction (OER).

The light that is taken in by the photoanode must have more energy than the semiconductor bandgap. After the formation of electron-hole pairs, the charge carriers are divided due to the electric field caused by band bending [10]. Holes move from the valence band (VB) to the surface of the photoanode, and electrons move from the conduction band (CB) to the CE. In the end, a portion of these carriers are effectively involved in HER and OER. The reactions occuring in an acid media are as follows.

Hydrogen evolution reaction (HER - cathode):

$$4H^+ + 4e^- \rightarrow 2H_2,\ E^0_{H^+/H_2} = 0\ V \tag{1.1}$$

Oxygen evolution reaction (OER - photoanode):

$$2H_2O + 4h^+ \rightarrow O_2 + 4H^+,\ E^0_{O_2/H_2O} = 1.23\ V \tag{1.2}$$

In order for the reactions to take place, a minimum energy of 1.23 eV is necessary, which is equivalent to a wavelength of light of around 1000 nm [9, 10]. This energy value is derived from the Gibbs free energy (ΔG^0) of the overall reaction (1.3):

$$2H_2O \rightarrow O_2 + 2H_2,\ \Delta G^0 = 238\ kJ \cdot mol^{-1} \tag{1.3}$$

Here, $\Delta G^0 = -nF\Delta E^0$, where n is the number of electrons involved in the reaction, the Faraday constant is represented by F, and the voltage difference is ΔE^0. For $\Delta E^0 = 1,23$ V, the reaction can take place, but this is the least amount of voltage needed. Taking into account the thermodynamic losses associated with carrier recombination, carrier transport resistance in the semiconductor, and the over-potential required for surface reaction kinetics [7], the actual energy required is approximately 1.8-2 eV [10].

1.3 Semiconductor Materials Used in Photoelectrochemical Cells

The choice of a suitable semiconductor is key for PEC water splitting. The main semiconductor properties to consider are as follows:

- A band gap that can capture the majority of natural sunlight is necessary for improved efficiency. Absorption of light in the visible spectrum is essential for this purpose [7].
- The band edge positions must take into account the potentials of PEC water-splitting reactions. Therefore, the valence band should be higher than the OER potential and the conduction band should be more negative than the HER potential.
- The solar spectrum reveals that sunlight intensity decreases significantly at wavelengths below 390 nm [11], leading to a maximum band gap energy of 3.2 eV.
- Maximizing carrier separation and transportation efficiency is critical to prevent charge recombination and accumulation [12].
- Materials that are effective, reliable, and capable of responding to light are necessary for water splitting powered by light [12].
- Semiconductors must be cost-effective, non-toxic, scalable, and plentiful to be viable for industry use [13].

The challenge of locating materials that meet the requirements is daunting. In 1972, Fujishima and Honda were the first to succeed in the water splitting process, using titanium dioxide (TiO_2) as the photoanode [14]. Metal oxides were then given more attention due to their excellent chemical stability. Subsequently, a variety of semiconductor materials have been used in water splitting systems. Figure 1.2 displays some of the most interesting semiconductors and their respective band gap energies.

Hematite (α-Fe_2O_3) [16], zinc oxide (ZnO) [17] and tungsten trioxide (WO_3) [18] are among the metal oxides reported. Hematite is one of the most studied materials due to its abundance as a semiconductor [19] and its narrow bandgap (2.2 eV) [13], which allows for great absorption of light within the solar spectrum. However, its low conductivity, low charge separation efficiency and high electron-hole recombination rate [20] necessitate the exploration of other materials or the implementation of techniques to improve its semiconductor performance. Comparably with hematite, WO_3 presents several advantages, such as a higher carrier lifetime, higher electron mobility, higher carrier concentration, long hole, and electron diffusion lengths, favorable energy band edge for oxygen evolution, high stability in acidic aqueous solutions and presents isotropic electronic properties, making it attractive for PEC applications.

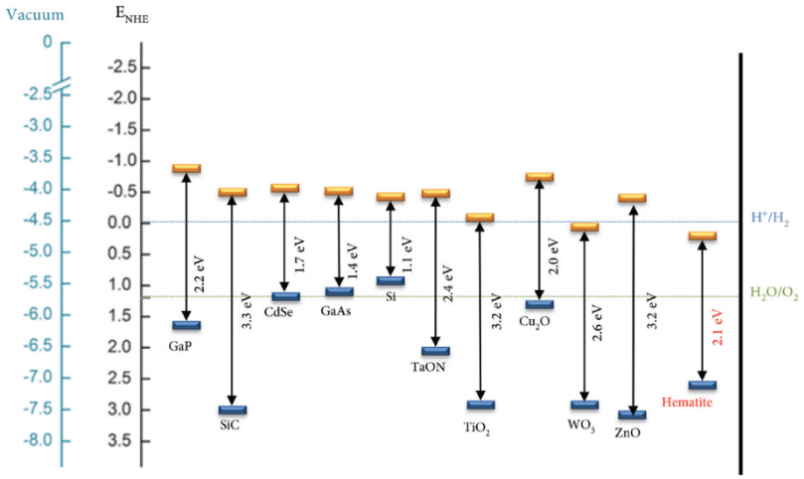

FIGURE 1.2: Band gap and corresponding edge positions of semiconductors in contact with an aqueous electrolyte at pH = 0 [15].

1.3.1 Tungsten Trioxide (WO_3)

This thesis examines the use of WO_3 as a photoanode for solar water splitting applications. Its first reported study as an alternative anode material dates back to 1976 [21]. Since then, it has been extensively studied due to its attractive chemical and physical properties. Among these n-type semiconductor properties, its chemical stability and high resistance to photocorrosion in aqueous media under different pH values [22] are two of the most important characteristics. Furthermore, its narrow band gap of 2.5-2.8 eV [23] allows for the absorption of up to 480 nm of solar radiation wavelength. Moderate hole diffusion length (≈150 nm) compared to other common semiconductor oxides, and fast electron transport (12 $cm^2 \cdot V^{-1} \cdot s^{-1}$)[24] appear as other significant properties as well. Although the WO_3 valence band potential is suitable for water oxidation, its small conduction band potential compared to the water reduction potential means that an external bias must be applied. With a theoretical maximum solar to hydrogen (STH) conversion efficiency of ≈6% [25], further research is needed to place this semiconductor in pair with other materials capabilities.

1.3.1.1 Structural Properties

Ideally, WO_3 has a cubic structure. However, its experimental observation is quite peculiar [26]. Its crystal structure is composed of a three-dimensional lattice of corner-connected WO_6 octahedra [27]. The W atom is located in the center of the octahedron,

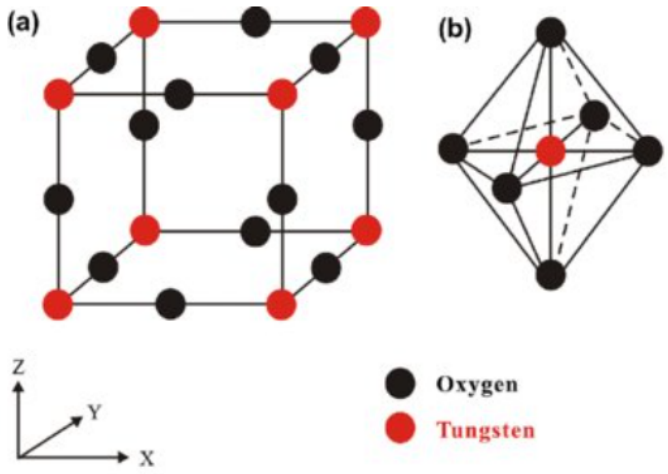

FIGURE 1.3: WO_3 structure. a) The ideal WO_3 cubic structure. b) The WO_6 octahedra [27].

while the O atoms are situated at the contact points between octahedrons [28] (Figure 1.3).

Depending on temperature, the WO_6 units alter either their tilt and rotation or the central location of the W atoms to lower symmetry crystal phases: monoclinic II (ϵ-WO_3, $<$ -43ºC), triclinic (δ-WO_3, -43ºC to 17ºC), monoclinic I (γ-WO_3, 17ºC to 330ºC), orthorhombic (β-WO_3, 330ºC to 740ºC) and tetragonal (α-WO_3, $>$ 740ºC) [27]. Hexagonal h-WO_3 has also been reported, however, when annealed at a temperature higher than 400ºC, it changes to the monoclinic I (γ-WO_3) phase [29].

At room temperature, the most stable crystal phase for bulk WO_3 is reported to be the monoclinic I (γ-WO_3) [26, 27]. In the case of nanostructured WO_3, some structures may preserve the orthorhombic crystal phase at room temperature [26], and phase transitions occur at lower temperatures than those of the bulk WO_3 [30].

Adding to these properties, the crystal lattice is capable of bearing oxygen vacancies [27]. These nonstoichiometric forms of tungsten oxide display varying colors, with WO_3 being yellow (Figure 1.4).

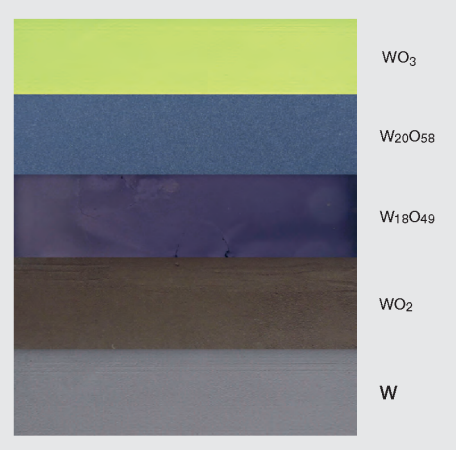

FIGURE 1.4: The colors of some tungsten oxides and respective stoichiometric proportions [31].

1.4 Photoanode Efficiency Improvement

1.4.1 Nanostructures

Recent advances in nanotechnology and nanoscience have demonstrated the potential to take advantage of novel physical and chemical characteristics when the size of the material is extremely small [32]. It has been confirmed that electrons can be confined to two, one or even zero dimensions in these structures, implying that the shape and size of nanomaterials can affect their properties [27]. Therefore, nanostructured WO_3 appears to be a feasible solution to address the reported photoelectrochemical issues. In comparison to the film and bulk structures, nanostructured materials have a larger electrode/electrolyte interface area and a shorter diffusion distance for minority carriers, which favors the separation and transfer of photogenerated carriers [33]. Furthermore, the porous morphology of nanostructured photoelectrodes enhances their light absorption ability, as the decrease in light reflection and the increase in the transmission path of light have been verified [32, 34]. Despite the many benefits, the reduced size of these structures can have a detrimental effect on the interaction with light in the visible spectrum, as well as leading to increased electron-hole recombination due to small crystal surface defects [12, 25].

The advantages of WO_3 have led to the development of a variety of nanostructures and fabrication techniques, such as nanoparticles created by spin coating [35], nanowires produced by the solvothermal technique [36], nanorods formed by the hydrothermal method [37], tree-like structures made by the pulsed layer deposition process [38], and nanopores generated by the anodization approach [39]. It is noteworthy that when the

same fabrication techniques are used under the same conditions to create various nanostructures, the semiconductor band gap energies can vary due to the different quantum confinement effects of the different nanomaterials [27, 40].

1.4.2 Electrochemical Anodization

The challenge of increasing photoconversion efficiency has made self-organized nanotubes (NTs) and nanopores (NPs) increasingly important. These nanostructures have a thin wall and high crystallinity, which helps reduce charge carrier recombination [40]. The most commonly used method to create highly ordered arrays of NPs and NTs is electrochemical anodization, which has been used to fabricate TiO_2 NTs, for example [41–43].

The anodization process involves the application of a voltage between the sample (working electrode) and a counter electrode (usually an inert metal such as platinum [Pt]). Both electrodes are placed in a suitable electrolyte, allowing the growth of NTs oxide. This synthesis technique can be carried out with basic laboratory materials at a low cost, making it attractive for large-scale systems.

The curves of the current density's evolution in time [$j(t)$] enable us to observe the different stages of NTs formation. Figure 1.5 shows the development of $j(t)$, its corresponding time derivative, and the thickness of the barrier layer for the W anodization. The high-field conduction theory states that the connection between j and the voltage (V) drop across the barrier layer thickness (δ_b) at the bottom of the NTs is as follows:

$$j = \alpha e^{\beta \frac{V}{\delta_b}} \tag{1.4}$$

where α and β are material-temperature dependent constants and the ($\frac{V}{\delta_b}$) ratio is the effective electric field across δ_b [44]. The physical similarities between TiO_2 and WO_3 suggest that the experimental values obtained for TiO_2 ($\alpha = 2.4 \times 10^{-9}$ mA·cm^{-2} and $\beta = 27.98$ nm·V^{-1}) [45] can be applied to WO_3. Rearranging equation 1.4, the δ_b value can be determined from the $j(t)$ curve as follows:

$$\delta_b = \beta \frac{V}{ln(\frac{j}{\alpha})} \tag{1.5}$$

Initially, due to a decreased electrical resistance across the electrodes and electrolyte, the current density denotes high values. However, a steep drop in j occurs until the j minimum value (j_{min}) is reached, indicating the formation of the tungsten (W) oxide layer.

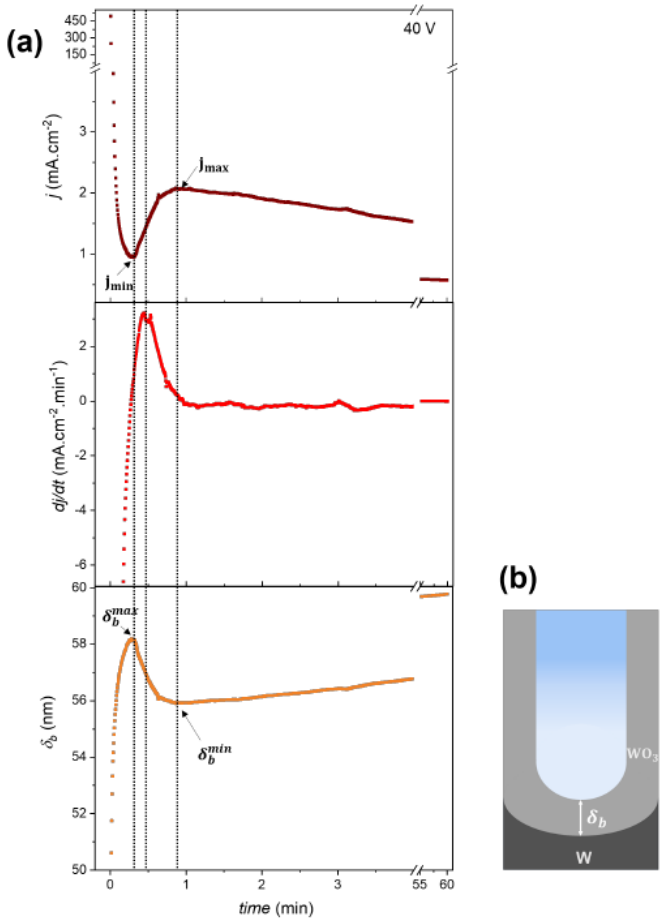

FIGURE 1.5: (a) (From top to bottom) Transient of the current density curve, respective time derivative and barrier oxide layer thickness evolution of W anodization at 40V. (b) Representation of the barrier oxide layer formed at the bottom of the NTs [40].

The presence of fluoride ions (F^-) is responsible for the etching pits on the oxide layer (created by the dissolution of the oxide) and results in a self-organizing porous structure, which explains why fluoride-containing electrolytes are so widely used for the formation of porous WO_3 [46]. The evolution of the barrier layer at the bottom of the NTs allows us to understand their growth behavior, with the maximum thickness (δ_b^{max}) being reached when the current density reaches j_{min}. After this, j increases until it reaches a maximum value (j_{max}), while the thickness of the barrier layer decreases to a local minimum (δ_b^{min}) as a possible consequence of the WO_3 dissolution dominance [40]. This stage is characterized by the nucleation of pores, which is enabled by the high electric field-driven dissolution of the oxide surface in the valley-type irregularities [47]. Subsequently, there is a slow evolution of the current density and an increase in δ_b.

The current density time derivative (dj/dt) enables a deeper understanding of the smaller effects in the NTs formation mechanisms. The commonly accepted notion that

j_{min} marks the beginning of NT nucleation [48] is not supported by the analysis of dj/dt, which does not show any alteration. Therefore, the decrease in the rate of the time derivative may be indicative of the formation of holes [40].

Studies of WO_3 growth through anodization have been conducted on NT and NP, and further research is necessary. Grimes et al. [49] were the first to report the formation of nanoporous WO_3 from W anodization. Since then, numerous studies have been conducted on the subject, resulting in improved PEC performances. According to Martins *et al*. [50], a photocurrent of 2.5 $mA{\cdot}cm^{-2}$ at 1.2V vs. Ag/AgCl/KCl was achieved in aqueous electrolyte containing 0.1M Na_2SO_4, yet this is still far from the maximum photocurrent of 4 $mA{\cdot}cm^{-2}$ that can be obtained under AM 1.5G solar illumination for a WO_3 photoanode [25]. Relevant information about this report is that photoelectrochemical characterization was performed under UV-vis illumination, which may lead to an overestimation of the real photoactivity of the anode due to increased light absorption of WO_3 in the UV spectrum. Similarly, other research works reporting anodic WO_3 photocurrents have not yet reached the theoretical maximum. For example, [51] achieved a photocurrent of 0.35 $mA{\cdot}cm^{-2}$ at 1V vs SCE in aqueous electrolyte with 1M H_2SO_4, under AM 1.5G 100 $mW{\cdot}cm^{-2}$ illumination conditions. Regarding the geometrical characteristics of anodic WO_3 NTs and NPs, the literature suggests pore diameters (D) in the range of 60-80 nm [50, 52, 53]. NPs/NTs oxide thicknesses (L) generally evidence values equal or less than 750 nm [50, 54, 55]. However, a recent dissertation work [56] claimed to achieve oxide thicknesses on the micrometer scale, a neverseen result for anodic WO_3 nanotube length grown by anodization, resulting in a photocurrent improvement.

1.4.3 Thermal Annealing

The amorphous WO_3 nanostructures and nanoparticles must be transformed into the crystalline phase in order to be useful for PEC applications. To achieve this, thermal annealing is applied, which involves exposing the nanostructure to high temperatures in a controlled environment. This process leads to a reorganization of the structure, with atoms adhering to preferential sites, resulting in a higher degree of crystallinity [28, 57].

As mentioned in Section 1.3.1.1, the typical crystal phase for bulk WO_3 at room temperature is the monoclinic I phase (γ-WO_3). Depending on the chosen annealing conditions, different effects are verified in the anodic WO_3 NTs/NPs. Nanoporous structure was found to collapse with high annealing temperatures, while at 600°C a complete loss of

morphology was reported [58]. In addition, the anodic oxide is completely different after thermal treatment, with reported higher thicknesses than at lower temperatures [57, 59]. On the other hand, at 400ºC the nanoporous morphology is preserved [59]. Once the nanoporous WO_3 is heated to 300°C, it transitions from an amorphous state to a monoclinic one. At 500°C, a dense oxide layer is formed beneath the nanoporous layer, as reported in [57]. Higher annealing temperatures generally produce nanoporous WO_3 with a higher degree of crystallinity [57]. However, given that at higher annealing temperatures the nanostructure exhibits a decreased surface area [57, 58], the photoresponse is reported to decrease with increasing annealing temperature [57]. In fact, in the case of WO_3 thin films, despite a higher degree of crystallinity obtained at 600°C, a decrease in photoresponse was reported for this temperature due to the reduced number of electrochemical reaction sites [60].

1.5 Electropolishing

Electropolishing (EP) can be used as a surface treatment on metallic surfaces prior to anodization in order to enhance the quality of semiconductor growth.

1.5.1 Theory and Working Principles

EP, also known as anodic polishing or electrolytic polishing, is a finishing process that removes material from a metal or alloy to improve its surface quality by reducing its roughness. This is achieved through anodic dissolution, which is the removal of ions from the sample surface one by one. Typically, the anodic metal workpiece, as well as the tool cathode, are immersed in the electrolyte. The tool cathode is an inert metal connected to the negative polarity, being the metal sample connected to the positive one. The power supply can either be DC or AC, generating current that flows between the electrodes (Figure 1.6).

Gas bubbles (normally hydrogen) seen at the cathode in figure 1.6 are the result of the reduction reaction caused by the electron flow, usually forming hydrogen [62]. On the anodic surface, metal atoms are converted to metal ions which are then dissolved into the electrolyte. EP is an appealing surface treatment process for complex-shaped samples since it uses an aqueous electrolyte as its polishing media. This contactless inter-electrode

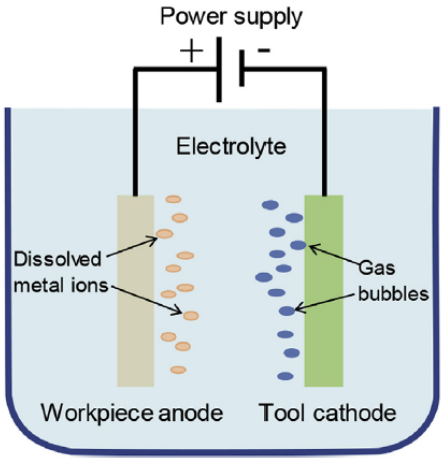

FIGURE 1.6: Schematic of EP process [61].

interaction does not cause any mechanical damage or stress to the anodic sample after EP has been applied [63].

The first discovery of this process and its operating principle can be traced back to the nineteenth century, when Faraday [64] observed it. The dissolution of materials in electrolysis can be explained by Faraday's first and second laws:

- The quantity of dissolved or deposited material is proportional to the electricity ($m \propto Q$, where m is the mass of dissolved or deposited material and Q is the amount of charge flowing)
- The amount of liberated substances by a certain electricity quantity is proportional to their chemical equivalent weight [65].

Electrolysis is part of not only the EP foundation but also the electrodeposition and dissolution methods [61]. However, despite Faradays' early achievement, it was not due to 1930 that EP started being systematically investigated to be used in pratical applications. Being first studied by Jacquet [66] to understand the dissolution process of anodic material, the voltage-current density curve (also named polarization curve) provides insight into the various stages involved in the EP process. Those include etching, passivating, polishing and gas evolution (figure 1.7).

In region I, the workpiece is dissolved directly (etching). This can lead to the formation of pits on the metal surface. The current will increase until it reaches a local maximum, at which point the behaviour is determined by the ohmic resistance of the electrolyte [68].

After the peak of the curve is reached, the current density gradually decreases until it reaches a steady level in region II. This is known as the passivating region, where an

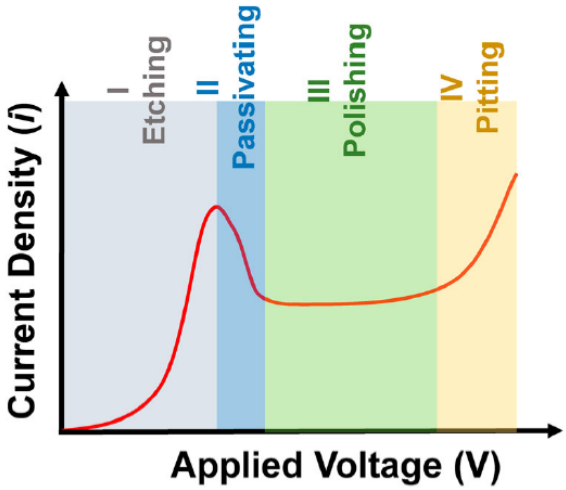

FIGURE 1.7: Current density-voltage curve representation of the general EP process [67].

oxide layer is formed on the anodic surface [61]. Region III represents the limiting current plateau region, where there is formation of a viscous layer that stabilises and allows metal ions to diffuse through it [67]. At higher voltages, this layer breaks down and oxygen forms bubbles on the anodic surface, leading to the gas evolution stage (region IV). This region is also known as the pitting region, as it is where pitting easily occurs [61].

EP is typically divided into two distinct surface treatments: macrosmoothing and microsmoothing. Macrosmoothing is the process of flattening out roughness heights greater than 1 micrometer, while microsmoothing is the elimination of surface heights less than 1 micrometer [62]. Three possible mass transport mechanisms have been proposed to explain microsmoothing:

- The dissolved metal cations diffusion control theory (electroneutrality is maintained by the electrolyte anions accumulation in the anodic diffusion layer due to dissolving metal cations saturation concentration at the anode) [62]
- The acceptor ions diffusion control theory (acceptor ions consumption at the anode by formation of complexes) [69]
- The water diffusion control theory (water molecules diffusion from the bulk to the anode to be consumed and form complexes with metal ions) [70]

Based on the mass transport mechanism, Jacquet [66] proposed the viscous film theory, one the most widely accepted theories to explain EP. Dissolved oxidation ions form a viscous liquid film with high viscosity and electrical resistance in the anodic surface. This film thickness oscillates according to the workpiece electrode height profile (greater at the

depressed parts, lower at the raised ones - figure 1.8). Therefore, metal ions concentration gradient is formed across the diffusion layer [71].

The acceptor ions present in the electrolyte diffuse through the viscous film and gradually remove the cations from the diffusion layer. If the anions react with metal ions as soon as they reach the surface, their surface concentration is zero at steady-state [67]. Since there is a metal ion concentration gradient, different ohmic resistances are verified across the diffusion layer. This leads to greater dissolution of the protruded surface parts, creating an uniform surface profile [73]. This theory was fundamental in the development of posterior ones for each type of metal, such as the WO_4^{2-} viscous film control theory for tungsten EP [74] and the diffusion theory for copper EP [75].

In recent times, various theories have been put forward to explain EP. Hoar *et al*. [76] proposed that a thin passive film is formed on the anodic surface, which is quickly dissolved by the electrolyte, making it difficult for the film to become thick. This differs from Jacquet's theory, which suggested that a viscous layer is located between the anodic surface and the bulk of the electrolyte. Hoar *et al*., however, proposed that the viscous layer is situated between the oxide layer (formed from the metal dissolution) and the bulk electrolyte.

A study has been conducted which proposes that two layers form on the metal surface [77]: a compact layer and a porous one. The pores of the porous layer are filled with electrolyte, allowing cations and anions to move, and thus enabling the current to flow. However, as the film has high electrical resistance, porosity is low and thickness is in the order of several microns [61]. As for the compact film, a solid high electric field dielectric barrier is formed, where cations flow by solid-state ionic conduction. The lower mobility of ions for solid-state transport means that this barrier is typically considered to be only a few nanometers thick[61].

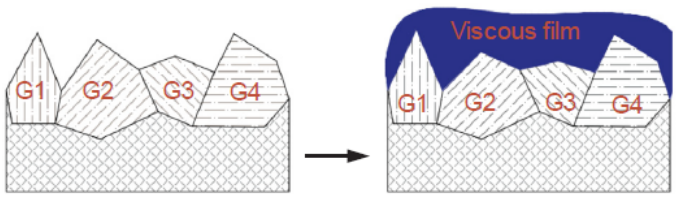

FIGURE 1.8: Viscous layer formation in the EP process [72].

1.5.1.1 Models for Tungsten Electropolishing

As mentioned in the previous section, the viscous film theory can be used to explain the anodic dissolution of tungsten [74]. This film is non-conductive and composed of WO_4^{2-}, which was formed when its generating rate was higher than its diffusion rate. The theory of controlling mass transport can also explain the dependence of the metal dissolution rate on the ion diffusion rate [74].

A combination of the aforementioned EP theories with the tungsten dissolution behaviors was reported [78]. Tungsten electropolishing can be broken down into four distinct stages: anisotropic etching, isotropic etching, merging of pits, and surface leveling. Figure 1.9 illustrates these phases.

The initial step of the process involves the breakdown of weak points in the protective coating on the anodic surface, which leads to the dissolution of tungsten at those areas. As the reaction products that make up the viscous layer have a low concentration, the layer is unable to become thick and anisotropic tungsten etching is observed (activation polarization state). This results in an increase in surface roughness. The etching pits then start to expand, allowing the viscous layer species to accumulate and thicken the film. This is the second stage of the process, where dissolution of tungsten enters the

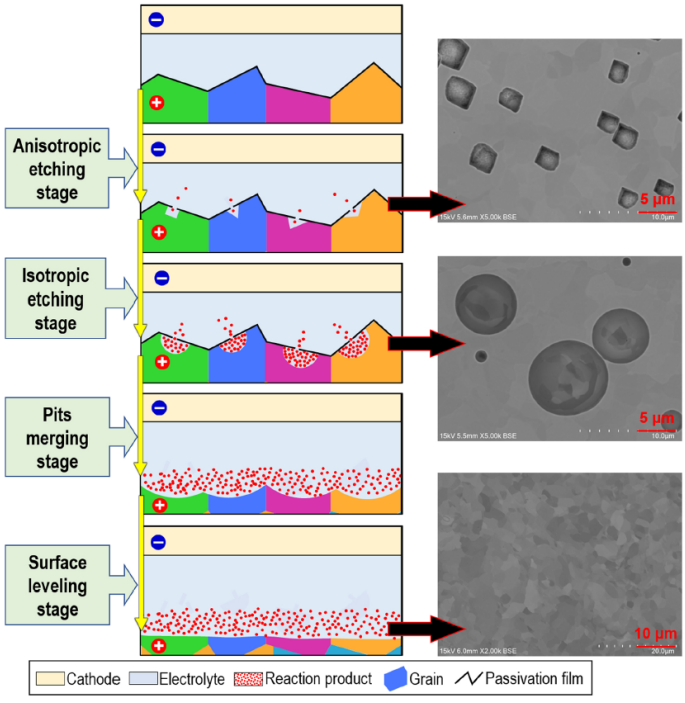

FIGURE 1.9: Sketch map of the tungsten EP process evolution, with illustrative SEM morphology top view images [78].

mass transfer polarization phase, and etching spots grow in regular shapes. Eventually, these pits join together, and the passivation film collapses. The anodic surface is now a smoother, pit-merged surface. In the final stage, the viscous layer on the surface becomes thicker and enables the surface to be levelled. Dissolution of tungsten is now regulated by the mass transfer process [78].

1.5.2 The Influence of Electropolishing Parameters

EP is a complex mechanism with many parameters capable of influencing its effectiveness. Some of them will be discussed in this section.

1.5.2.1 Electrolyte Composition

Acting as a current, heat and reaction carrier, electrolytes are an integral component of EP, with electrolyte conductance as the main characterization property [67].

Typically, a highly viscous, concentrated acid mixture is selected, such as a perchloric acid-acetic acid solution [62], which has been used for the production of high-purity aluminium EP [79]. Nevertheless, this may not be the best choice for a tungsten workpiece electrode. Studies comparing acid to basic electrolytes in tungsten EP were conducted [72, 78]. For the acid media composed of H_3PO_4 and glycerol in solution, the equations describing the electrochemical reactions taking place are the following:

$$Cathode : 2H^+ + 2e^- \longrightarrow H_2(g) \tag{1.6}$$

$$Anode : W(s) + 3H_2O \longrightarrow WO_3(s) + 6H^+ + 6e^- \tag{1.7}$$

$$WO_3(s) + H_2O \longrightarrow H_2WO_4(aq) \tag{1.8}$$

Equation 1.8 refers to the dissolution of the oxide film layer, which is quite slow. Consequently, the material removal rate is slow as well [72]. Concentration of the limitation carriers that take part in mass transport limitation in the viscous film layer is believed to be the EP controlling factor in this type of electrolytes [61]. On the other hand, NaOH electrolyte was chosen for the basic electrolyte setup. The equations representing the electrochemical processes occuring in each electrode change:

$$Cathode : 6H_2O + 6e^- \longrightarrow 3H_2(g) + 6OH^- \tag{1.9}$$

$$Anode : W(s) + 6OH^- \longrightarrow WO_3(s) + 3H_2O + 6e^- \tag{1.10}$$

$$WO_3(s) + 2OH^- \longrightarrow WO_4^{2-} + H_2O \tag{1.11}$$

In contrast to the system with the acidic electrolyte, the dissolution of WO_3 as described in equation 1.11 is rapid [72]. Even before the EP process begins, an oxide layer formed by air is already present on the metal. Subsequently, reactions 1.11 and 1.8 are believed to occur first in tungsten EP [72]. Due to the higher dissolution rate in reaction 1.11 and low NaOH viscosity, EP reveals a higher plateau of limiting current density for the setup with NaOH, and it is unlikely that a thick viscous film layer is formed [72]. An important aspect to consider as well is the electrolyte pH value, which should be higher than or equal to 10 so that the only reaction occurring in the process is the tungsten dissolution [80].

1.5.2.2 Stirrer Speed

A rotating piece can be added to the EP setup in order to improve EP treatment. Comparing different rotation speeds, it was found that higher values decreased the diffusion layer thickness and, as a consequence, a shorter path length for the diffusion of ions was verified for anodic NiTi alloys [81]. This lead to an increase in the limiting current plateau height [81]. The same observation was reported for niobium [68]. It is necessary to investigate the ideal value for each material, as the surface quality begins to deteriorate at very high rotation speeds due to the excessive removal of the viscous film [82]. To the best of our knowledge, there is no report on the optimization of the stirring speed for tungsten EP.

1.5.2.3 Time

Previous research has indicated that the amplitude of a surface profile tends to decrease exponentially as the EP time increases [83–85]. However, when tungsten is the material being polished and the electrolyte is 2 wt% NaOH, the surface roughness may not follow an exponential pattern for EP times shorter than 30 seconds [78]. This tendency was once

again verified for EP times lower than 10 seconds in an acid media EP [78]. Despite this, these EP time ranges are not applicable, as pitting occurs on the anodic surface for such short EP times [78]. For longer time values, the exponential tendency is valid [72, 78].

1.5.2.4 Temperature

Temperature increase in EP was found to increase the limiting current plateau in Niobium EP [68, 86]. The same findings were reported for stainless-steel EP [70]. Despite this, it is essential to be aware that an increase in temperature results in a decrease in the viscosity of the anodic diffusion layer [67], which weakens the viscous layer. This has a direct impact on the quality of the surface treatment. Therefore, it is recommended to conduct a thorough study of the EP temperature for each material. No literature was found that discussed the optimization of the EP temperature for tungsten.

1.5.2.5 Potential

The potential selected to perform EP is usually restricted to the limiting current plateau voltage range [61], which varies depending on the anodic material. Regarding tungsten EP, the etching stage is reported to be in the 0-5V potential range and the limiting current plateau in the 5-25V range [74].

Chapter 2

Experimental Techniques

This chapter provides an overview of the experimental methods and materials used. First, the materials and reagents are discussed, followed by the fabrication techniques of nanostructured WO_3. Lastly, the characterization techniques used to analyze the samples are outlined.

2.1 Materials and Reagents

Nanostructured WO_3 was obtained from high-purity W foil (99.95%) with a thickness of 0.1 mm, sourced from Alfa Aesar and Thermo Scientific.

This section details the reagents used experimentally, as well as their chemical formula, supplier company and purity.

Substrate and Anodization Cell Cleaning:

C_3H_6O, Acetone (Valente e Ribeiro. Lda, 99% Vol.);
C_2H_6O, Ethanol (Valente e Ribeiro. Lda, 99% Vol.);

Electropolishing Electrolyte:

NaOH, Sodium Hydroxide (LabKem, $\geq$ 98.0%);

Anodization Electrolyte:

NH_4F, Ammonium Flouride (Alfa Aesar, 98.0% min);
Na_2SO_4, Sodium Sulfate (Acros Organics, 99+%).

2.2 Methods

2.2.1 Substrate Cleaning

Before undergoing electropolishing and electrochemical anodization, W samples were pretreated in an ultrasonic bath with acetone, ethanol and deionized water, in that order, for a period of 10 minutes each.

Once the procedures were completed, the samples were washed with ethanol and deionized water and then allowed to air dry.

2.2.2 Electropolishing

A home-made EP setup was used to carry out W electropolishing (Figure 2.1). The counter electrode (cathode) was a rectangular Pt mesh, and the W sample was the working electrode (anode). Both electrodes were submerged in the electrolyte and connected to a Keithley 2004 Sourcemeter DC power supply, which was operated by a custom-made LabView application [40]. The voltage and EP time were set in this program, and the evolution curves of the current density were automatically recorded.

FIGURE 2.1: Photograph of the electropolishing setup used.

All experiments were conducted at room temperature and under constant potential. The size of the anodic sample area in contact with the electrolyte, the gap between the electrodes, and the speed of the electrolyte stirrer were adjusted depending on the desired

study. The pH value of the electrolyte was maintained at a minimum of 10, as suggested in the literature [80].

2.2.3 Electrochemical Anodization

Once again, a low-budget setup was constructed to perform W anodization (Figure 2.2). The anodization cell is made up of a round Teflon container that is attached to a copper plate with screws, making sure that it is in contact with the W sample that is situated in between. An inert Pt mesh electrode is placed at the top and acts as the counter-electrode (cathode), while the W sample is the working electrode (anode). In a similar fashion to the EP setup, both electrodes were immersed in a suitable electrolyte and connected to a Keithley 2004 Sourcemeter DC power supply, which was managed by a custom-made LabView application [40]. The voltage, time, number of samples and sample diameter were adjusted in this application, and the current density evolution curves were automatically stored.

The anodizations were done at room temperature, with a constant voltage of 40V for a period of 60 minutes in a aqueous electrolyte containing 1M Na_2SO_4 and 0.5 wt% NH_4F. The speed of the stirrer and the size of the sample were adjusted according to the research conditions.

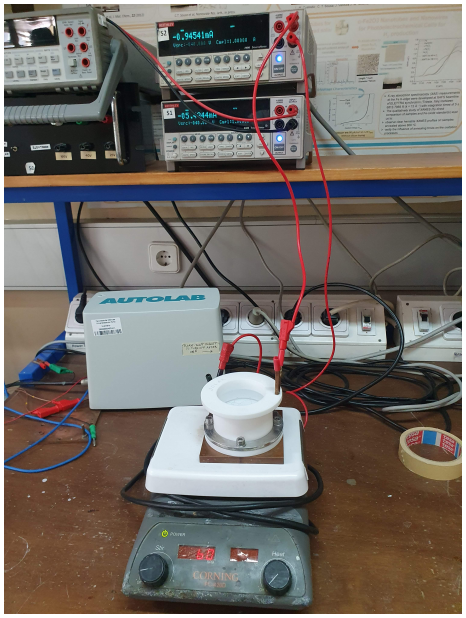

FIGURE 2.2: Photograph of the anodization setup used.

2.2.4 Thermal Annealing

After anodization, some samples were chosen to be thermally annealed. According to a dissertation [40], 500ºC was one of the temperatures used. To reach this temperature, the samples were heated gradually with an initial heating ramp. It has been reported that a slow-heating ramp annealing in multilayered WO_3 nanoplatelets increases the photocurrent density [87]. Therefore, as 2ºC/min is an already reported value [40, 58], 1ºC/min and 2ºC/min were the heating ramp values chosen for this study.

The failure to maintain the nanoporous structure at 600°C when annealing with a 2°C/min heating ramp [58] prompted annealing with 600°C and 1°C/min to investigate whether the heating rate had an effect on the morphology and degradation of the sample. All samples that were thermally treated were exposed to air, kept at the set annealing temperature for two hours [40, 58], and allowed to cool down to room temperature naturally.

2.3 Characterisation Techniques

2.3.1 Atomic Force Microscopy

Characterized as a high resolution surface microscopy technique, Atomic Force Microscopy (AFM) is a mechanical microscope. Invented in 1986 [88], it is composed of 4 main components: probe (combination of a cantilever and a sharp tip), optical lever, and piezo-XYZ scanner. The force between probe and surface is carefully kept constant along the scanning. Due to this force at the tip, the cantilever deflects vertically, with a laser focused on its back that detects these deviations [89]. The cantilever reflects this laser beam, which is then directed to a photodetector. As the laser spot moves across the photodetector, it provides a more accurate measurement of the probe's movement. This system is referred to as an optical lever. The sample is scanned by a scanner that has a piezoelectric element, enabling movements with increased precision [89].

When a laser beam is reflected onto a divided photodiode, the microscope is in Tapping Mode. By distinguishing the differential signal between the top and bottom photodiode sections, a precise evaluation of the cantilever deflection is made possible. The root mean square (RMS) value of the fluctuating cantilever deflection signal along the sample is determined using an analog circuit, which is equivalent to the amplitude of the cantilever oscillation [89]. This is a major breakthrough in AFM technology for imaging of functionalized surfaces [90].

This thesis employed the Tapping Mode of the Atomic Force Microscope (AFM) to conduct a surface topography analysis of W samples before anodization. The Nanoscope Multimode AFM from Veeco Instruments was used at the Centro de Microscopia da Universidade do Porto (CEMUP).

2.3.2 Scanning Electron Microscopy

Examining objects with Scanning Electron Microscopy (SEM) allows for the profiling of structures with a resolution of less than one micron, as well as obtaining the chemical composition of the sample.

A typical SEM setup consists of four main components: an electron gun (which is a combination of an electron source and an accelerating anode), electromagnetic lenses (which are responsible for focusing the electron path), a vacuum chamber (which houses the specimen being examined) and signal detectors [91] (Figure 2.3).

This system utilizes a focused electron beam to acquire data and form images. It can be moved along the sample or kept stationary over a small area to obtain specific information. The sample and electron beam interact to create a range of signals (see Figure **??**) that can be obtained from different parts of the sample.

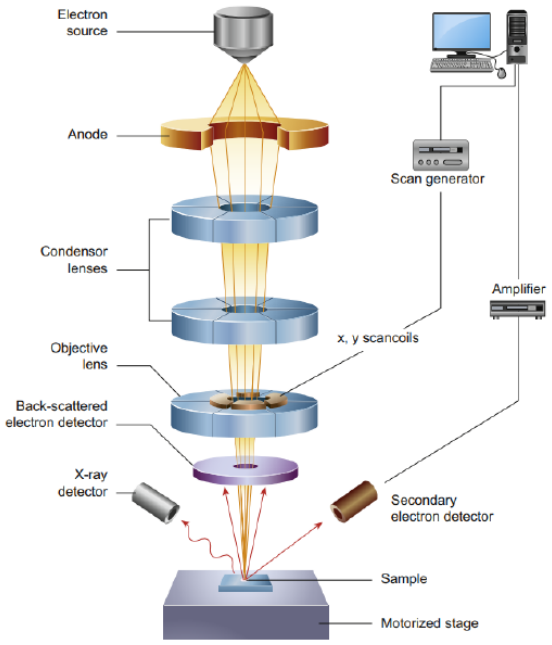

FIGURE 2.3: Schematic representation of the Scanning Electron Microscope main components [92].

The interactions between the incident electrons and the sample can be divided into two categories: elastic and inelastic. Backscattered electrons (BSE) are those that have a high energy and are elastically scattered at an angle greater than 90°, which is used for imaging and determining the chemical composition [93]. On the other hand, secondary electrons (SE) have a lower energy and are the result of inelastic interactions, which are used to obtain the topography of the sample [91]. Characteristic X-ray emission can be identified when a primary electron collides with an inner shell electron, in an effort to restore charge balance [40]. The energy of the X-ray emission is related to the chemical composition of the sample [92].

All morphological characterization was performed using a Phillips-FEI/Quanta 400 FEG high resolution scanning electron microscope (SEM), at the Materials Center from University of Porto (CEMUP). Samples were affixed to a sample holder with carbon tape. To capture top view SEM images, we simply laid the samples flat on the holder. For cross-section view, the samples were folded across the middle with the help of pincers. After the images were taken, measurements of the nanostructures' geometrical features, such as pore diameter (Dp) and oxide thickness (L), were taken using the open software ImageJ.

2.3.3 X-Ray Diffraction

It is essential to be aware of the crystallographic properties of the nanostructures that have been grown. This was discussed in the preceding chapter. X-Ray Diffraction (XRD) is a suitable method for obtaining information such as crystal structure, crystallinity, preferential growth directions, crystallite size (D) and microstrain (ϵ).

XRD is a technique used to analyze the structure of solid-state materials. It does this by measuring the interactions between the electrons in the atoms of the sample and the X-Ray beam. This causes radiation scattering, which has a wavelength that is similar to the lattice parameters of crystalline samples. Thus, the interference of scattered waves is verified, resulting in a diffraction pattern with constructive or destructive interference [94].

Constructive interference happens at certain angles that are connected to the distance between atomic planes (d_{hkl}) according to Bragg's law [95] (equation 2.1 and Figure 2.4).

$$n\lambda = 2d_{hkl}\sin\theta \tag{2.1}$$

The incident radiation λ is the wavelength of the interplanar distance d_{hkl} and the diffraction angle θ is the angle between the incident and scattered wave fronts.

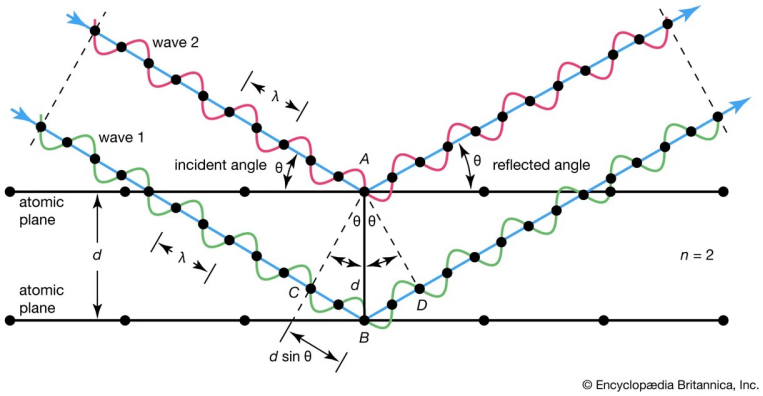

FIGURE 2.4: Geometrical representation of Bragg's Law, for n=2 [96].

Using Scherrer's equation, the average crystallite size (D) can be estimated from the diffraction pattern [32] (equation 2.2).

$$D = \frac{K\lambda}{\beta \cos\theta} \tag{2.2}$$

where K is the Scherrer constant (0.94), 2θ is the peak diffraction angle, λ is the wavelength of the X-ray radiation, and β is the full width at half-maximum (FWHM) of the diffraction peak [32].

In this thesis, XRD measurements were performed using the Bragg-Brentano $\theta - 2\theta$ with grazing incidence omega angle configurations. The SmartLab Rigaku diffractometer (Figure 2.5) present at IFIMUP was used, which consists of cooper Cu Ka radiation with a wavelength of 1.540593 $\AA$ and an x-ray tube with an anode at 200mA and 45kV.

2.3.4 Photoelectrochemical Characterization: Photocurrent Density-Voltage Curves

The photocurrent density - voltage (J-V) curve can be used to perform the PEC characterization and quantitatively analyze the photoperformance of a photoanode. The number of photogenerated charge carriers that participate in water oxidation and reduction reactions is proportional to the photocurrent density values, which are linked to the hydrogen production rates [97].

The setup for PEC photocurrent measurements used was a three-electrode configuration (Figure 2.6). A cappucino cell with an illuminated surface area of 0.528 cm^{-2} was

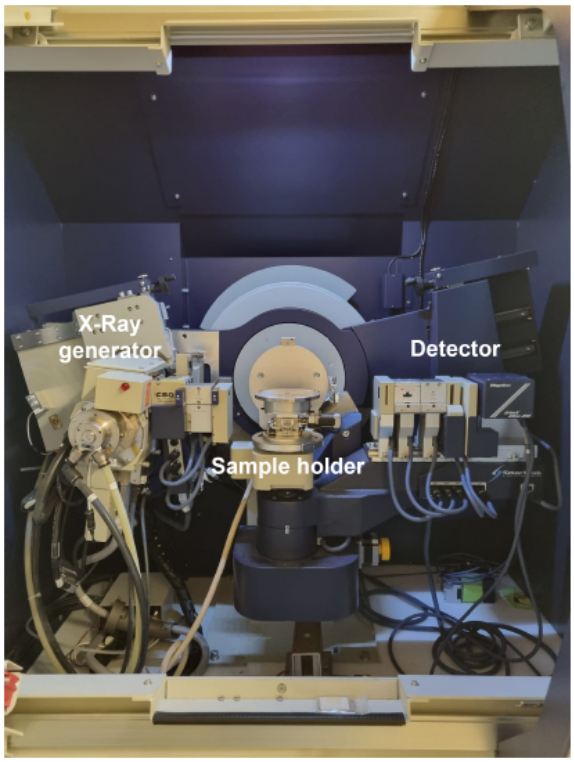

FIGURE 2.5: Rigaku SmartLab XRD (at IFIMUP) and its main components [40].

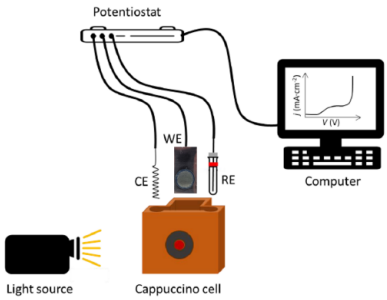

(A)

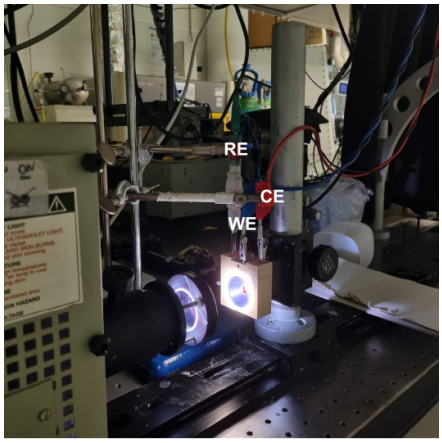

(B)

FIGURE 2.6: a) Schematic representation of j-V measurement system [94]. Photographs of measurement with a solar simulator under b) 1-sun light [40].

utilized. The WO_3 photoanode was the working electrode, with a Pt wire (Alfa Aesar, 99.9%) as the counter electrode and a Ag/AgCl/saturated KCl (Metrohm, Switzerland) reference electrode. The electrodes were immersed in a 0.5 M Na_2SO_4 electrolyte solution and the experiments were conducted in the dark and in the presence of 1 sun AM 1.5G light ($100 mW \cdot cm^{-2}$) [98], using a light simulator composed of a 150W Xe lamp (Oriel, Newport) that was calibrated with a c-Si photodiode.

The conversion of the measured potential vs Ag/AgCl electrode to the reversible hydrogen electrode (RHE) is achieved with the Nernst equation [94] (equation 2.3).

$$E_{RHE} = E_{Ag/AgCl} + 0.059pH + E^0_{Ag/AgCl} \tag{2.3}$$

where $E^0_{Ag/AgCl}$=0.1976V at 25ºC, $E_{Ag/AgCl}$ is the potential measured experimentally and pH = 6.17 is the pH of the electrolyte solution.

The J-V curves were registered using a potentiostat attached to the PEC cell, a ZENNIUM (Zahner Elektrik, Germany) workstation, together with the Thales software for data acquisition, at a scan rate of 10 $mV \cdot s^{-1}$.

Chapter 3

Tungsten Foils Electropolishing Optimization

In this thesis, WO_3 is produced from commercially available W foil by anodization. To improve the quality of the substrate, electropolishing (EP) of W is applied. A comprehensive study of tungsten EP is conducted. This method has a variety of parameters to investigate. First, a polarization curve analysis is performed to determine the tungsten EP voltage range and the most suitable stirrer speed. Then, the electrolyte concentration is optimized to reach an ideal value. Lastly, the applied voltage and EP time are examined. The resulting anodic WO_3 growth mechanisms, growth rates, and morphology will be affected by the EP process.

3.1 Experimental Details

Before electropolishing, the W foil pieces were ultrasonically cleaned in acetone, ethanol and deionized water for 10 minutes each step. Temperature was kept constant throughout this study (room temperature). EP was carried out in a setup similar to that described in Section 2.2.2.

3.1.1 Voltage-Current Density Curve Study

The electrolyte used was 0.5M NaOH [72, 78], and the surface area of the W sample in contact with the electrolyte was approximately 0.2 cm^2. Considering the values reported in [78] and [74], the gap between the electrodes was set to 2.5 cm. For the initial polarization curve analysis, there was no stirring speed (0 rpm).

3.1.2 Electrolyte Concentration Optimization

Table 3.1 presents the EP conditions considered for the electrolyte concentration optimization study. The choice of electrolyte concentration values was based on previous research [72, 78], as well as the voltage, distance between electrodes and time [78]. The stirrer speed was optimized from the study described in Section 3.1.1 and the contact area between the tungsten sample and the electrolyte was set at 0.9 cm^2.

Sample	Electrolyte	Potential (V)	Time (min)	Inter-electrode distance (cm)	rpm
EP1	0.125M NaOH	10	30	0.6	0
EP2	0.5M NaOH	10	30	0.6	0

TABLE 3.1: Electrolyte concentration optimization study conditions.

3.1.3 Applied Voltage and Time Optimization

The parameters for the applied voltage and EP time optimization study are presented in Table 3.2. Two applied voltage values were selected within the limiting current plateau potential range. The speed of the stirrer and the electrolyte concentration were optimized in Sections 3.1.1 and 3.1.2, respectively, while the inter-electrode gap was established according to tungsten EP studies reported in [78]. The maximum EP time was chosen based on the same article, with the sample area in contact with the electrolyte set at 0.9 cm^2.

Sample	Applied voltage (V)	Time (min)
EP3	10	2
EP4	10	10
EP5	10	60
EP6	15	2
EP7	15	10
EP8	15	60

TABLE 3.2: Summary of the group of samples with different EP Applied potential and time conditions for 0.125M NaOH, inter-electrode distance 0.6 and with no agitation (0rpm).

3.2 Voltage-Current Density Curve Study

Electropolishing typically takes place in the limiting current plateau region [61, 67]. Therefore, by identifying this region in the curve, one can have a range of applied voltage values that can be used to find the optimized tungsten EP voltage. Figure 3.1 shows the voltage-current density curve [$j(V)$] obtained and the respective time derivative (dj/dt). The

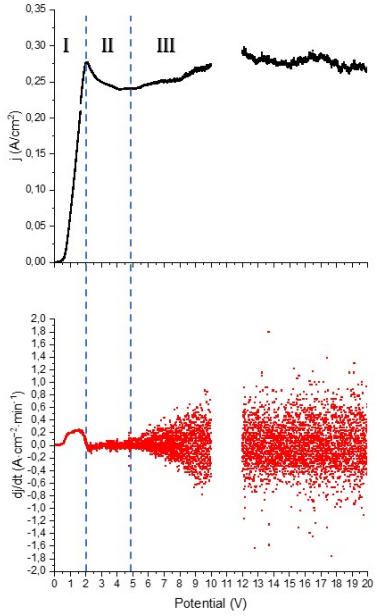

FIGURE 3.1: Current density-voltage curve of W EP and respective time derivative.

three regions of the curve, I, II and III, correspond to the EP phases discussed in Section 1.5.1: etching, passivating, and polishing, respectively.

In Region I (0-2V), the current density increases until it reaches a local maximum at 2V, with the time derivative initially increasing and then decreasing until it reaches 0. Region II (2-5V) is the passivating stage, where the mean time derivative of the current density is -0.011 $A \cdot cm^{-2} \cdot min^{-1}$, indicating a decrease in current. Region III (5-20V) is the limiting current plateau phase, where the current stabilizes, as confirmed by the mean time derivative of the current density being approximately 0 (5.2E-4 $A \cdot cm^{-2} \cdot min^{-1}$). The potential range 10-12V does not have any data representation (Appendix A). The pitting stage is not adequately depicted. The plateau region appears to be situated between 5 and 20 V, which is in agreement with the findings reported in Section 1.5.2.5. Restricting the possible applied potentials to this region, the stirrer speed was adjusted to maximize its effect on the polarization curve. The polarization curves for 0 rpm, 170 rpm and 400 rpm are shown in Figure 3.2.

An increase in the speed of the stirrer leads to an increase in the height of the plateau of the limiting current (regions 2, 4 and 5). This is in agreement with the reports by Wei and Han [61], stating that an increase in the rotation speed can reduce the thickness of the anodic diffusion layer, allowing ions to diffuse more easily due to a shorter path length.

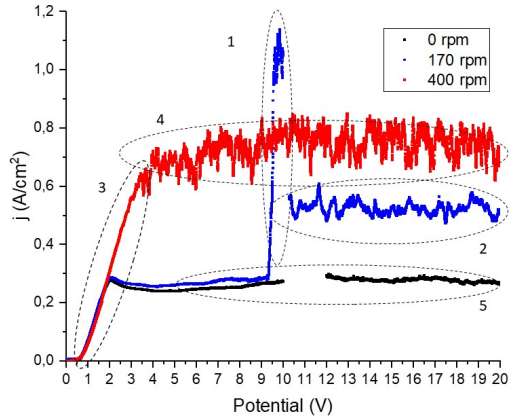

(A)

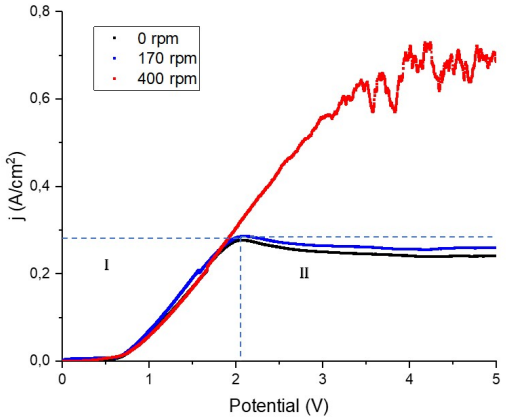

(B)

FIGURE 3.2: Polarization curves of W EP with 0.5M NaOH for stirrer speeds 0 rpm, 170 rpm and 400 rpm in the potential range a) 0-20V and b) 0-5V.

For 0 rpm, all EP phases are easily identified, and the voltage range of the plateau of the limiting current is large and stable (region 5; the curve for this stirrer speed was already analyzed in Figure 3.1). In the case of 170 rpm, the trend of the curve is similar to that of the 0 rpm one from 0-9V, with regions I and II showing the etching and passivating phases, respectively, for both speeds. Generally, the EP surface tends to be smoother as the current increases [99], [100]. However, region 1 reveals that, from 9-10V, there is a sharp increase in current density for 170 rpm, which confirms the suggested notion of excessive removal of the viscous layer for high rotational velocities reported in Section 1.5.2.2. Subsequently, a stable but dispersed current density behavior is observed for the remaining potential range in region 2 (10.3-20V). Regarding the 400 rpm curve, it can be seen that only two stages are present: etching (region 3) and polishing (region 4), with the

passivating phase not being explicit. Similarly to the observations for the 170 rpm curve, inherent noise in the polishing stage is visible (region 4).

Taking into account this analysis, the low thickness of the anodic metal (0.1 mm) and the contact area of the anodic surface and electrolyte ($\sim$0.2 cm^2 for this study; $\sim$0.9 cm^2 for the following analysis), the stirrer speed chosen for the EP study was 0 rpm.

3.3 Electrolyte Concentration Optimization

Figure 3.3 illustrates the EP results obtained for W samples at different electrolyte concentrations. The 0.125M NaOH electrolyte setup appears to have a smoothing effect (dark region), contrasting with the dull surface obtained when the sample is exposed to the 0.5M NaOH electrolyte.

The SEM top-view morphology of samples EP1 and EP2 is depicted in Figure 3.4, along with a top-view image of the W sample without EP for comparison.

EP1 (0.125M NaOH) has a noticeably smooth surface compared to the original W sample without EP, with the gray shading revealing the grain boundaries of tungsten. This is an example of defect removal, as the sample without EP has some irregularities that make it difficult to identify the grains. EP2 (0.5M NaOH), on the other hand, appears to have been heavily etched compared to the sample without EP, with different etching levels throughout the sample. To gain a better understanding of these results, one can examine the current density time evolution associated with the EP (Figure 3.5).

The current density curves demonstrate distinct trends. The W sample exposed to the 0.5M NaOH electrolyte shows saturation throughout the entire EP process. On the other hand, the setup with the 0.125M NaOH electrolyte displays a rapid increase in current followed by a sharp decrease. This behavior is indicative of the formation of a viscous

(A) (B)

FIGURE 3.3: W EP results obtained using 10V, 30 minutes and 0 rpm for a) 0.125M NaOH electrolyte and b) 0.5M NaOH electrolyte.

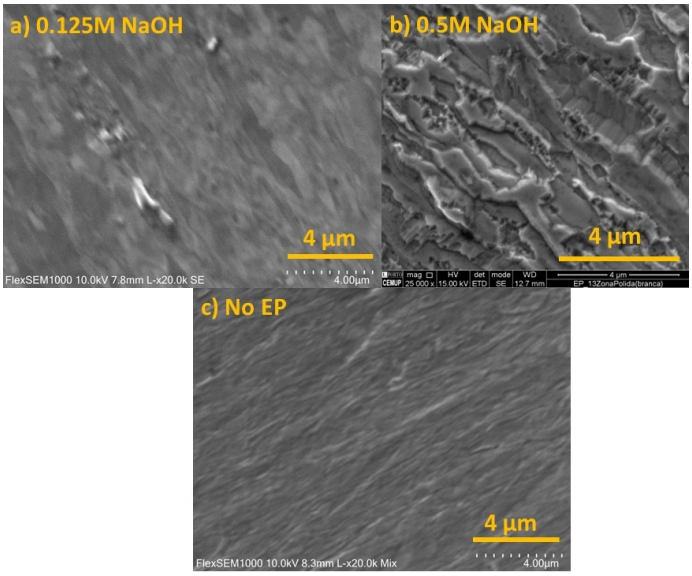

FIGURE 3.4: SEM top view morphology images of W samples after EP with 10V, 30 minutes and 0 rpm for a) 0.125M NaOH electrolyte and b) 0.5M NaOH electrolyte. For comparison, sample c) without EP is also represented.

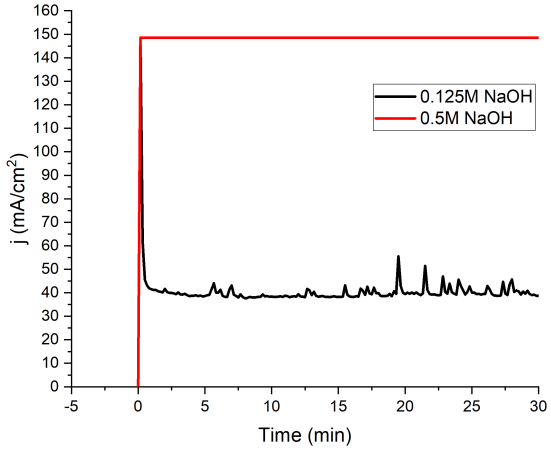

FIGURE 3.5: Current density evolution of W EP with 0.125M NaOH and 0.5M NaOH electrolytes. EP performed with 10V, 30 minutes and 0 rpm.

film, typical of a well-controlled EP process as discussed in Section 1.5.1 [74, 78]. The subsequent plateau of current density is the result of the equilibrium between ion diffusion and metal dissolution, implying that the thickness of the viscous film is constant [74].

The electrical conductivity of the 0.5M NaOH electrolyte setup is high, indicating that the viscous film layer is either very thin or non-existent. This is in agreement with the anodic dissolution model of tungsten proposed by Rong [78], which suggests that the viscous layer is minimal in the initial anisotropic etching stage due to the low concentration of reaction products on the anodic surface. This results in the formation of etching pits

and an increase in surface roughness. However, the current density does not experience any steep drop, suggesting that the system did not enter the mass transfer polarization stage and that etching occurred continuously. This is further supported by the top view SEM morphology image in Figure 3.6, which also shows anisotropic etching along the sample according to the crystallographic orientations of tungsten.

Moreover, for small distances between electrodes, higher concentration electrolytes have fewer localization effects [101] (electrochemical dissolution that is localized). Taking into account that the anodic dissolution process is more intense when the distance between the anode and the cathode is smaller and that higher concentration electrolytes increase the effective inter-electrode gap [72], a less effective EP is anticipated for the 0.5M NaOH electrolyte.

In conclusion, the 0.125M NaOH electrolyte revealed to be the most suitable solution for an optimum EP procedure and for that it was the electrolyte chosen.

3.4 Applied Voltage and Time Optimization

Figure 3.6 represents the SEM top-view morphology images obtained for samples EP3 (10V, 2 minutes), EP4 (10V, 10 minutes), EP5 (10V, 60 minutes), EP6 (15V, 2 minutes), EP7 (15V, 10 minutes), and EP8 (15V, 60 minutes), as described in Table 3.2.

The samples that underwent EP demonstrate a smoother surface than the one without EP, as was previously discussed in Section 3.3. The crystallographic grains become more visible after EP, evidenced by the gray-colored gradation in the EP samples. This gradation appears to be more distinct with increasing EP time, with samples EP5 (10V, 60 minutes), EP7 (15V, 10 minutes) and EP8 (15V, 60 minutes) exhibiting a better EP effect. For the same potential, a smoother surface is obtained with a longer EP time for both voltage values. However, EP4 (10V, 10 minutes) appears to have defects, which can negatively affect the quality of the subsequent nanotube growth when anodization is applied. Samples with the same EP time but different applied potentials appear to have a quite similar surface.

In order to supplement the morphology analysis, Atomic Force Microscopy (AFM) was used to have more detail of the micro surface in terms of topography and roughness. Figure 3.7 displays representative AFM images of the W samples.

The EP with 10V and 2 minutes exhibits a relatively uniform dimple pattern, which is a characteristic of metal EP [102]. For the EP with 15V and 2 minutes, a wave-patterned

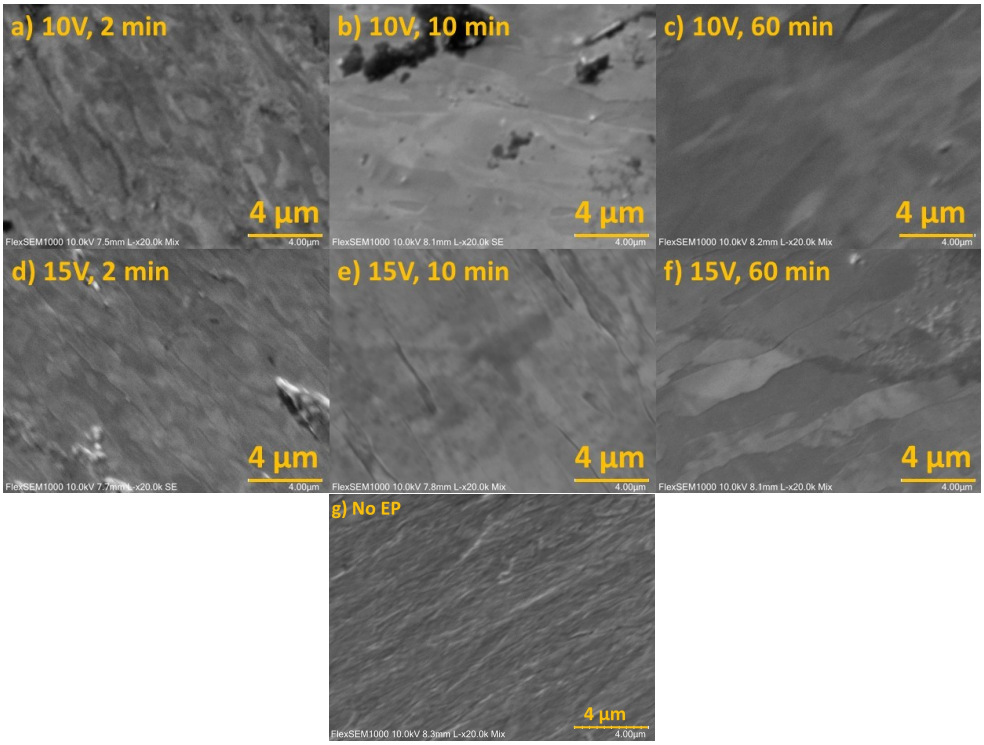

FIGURE 3.6: SEM top view morphology images of W samples after EP with 0.125M NaOH electrolyte, 0 rpm and a) 10V and 2 minutes (EP3), b) 10V and 10 minutes (EP4), c) 10V and 60 minutes (EP5), d) 15V and 2 minutes (EP6), e) 15V and 10 minutes (EP7), f) 15V, 60 minutes (EP8). W sample g) without EP also added for comparison.

surface is visible, with less distinct ripples and wider spaces between them than in the previous EP. This wave-like appearance is also present in the EP with 15V and 10 minutes, although the amplitude of the waves is much lower, resulting in a smoother surface with color shadowing. Regarding the EP with 10V and 10 minutes, some small indentations can be seen on a smooth surface without any discernible pattern. The same behavior is observed in the EP with 10V and 60 minutes, but with fewer dimples. The sample that appears to have the most smoothing effect is the EP with 15V and 60 minutes, with very few ripples and a flat surface. The as-rolled sample reveals a very unorganized and nonuniform surface, contrasting with the findings on the EP surfaces.

Based on the AFM images obtained in Figure 3.7, the root mean square surface roughness (R_q) was calculated. It is defined as the root mean square value of the height of the image pixels (equation 3.1) [103]:

$$R_q = \sqrt{\frac{1}{N}\sum_{i=1}^{N}(z_i - \bar{z})^2} \tag{3.1}$$

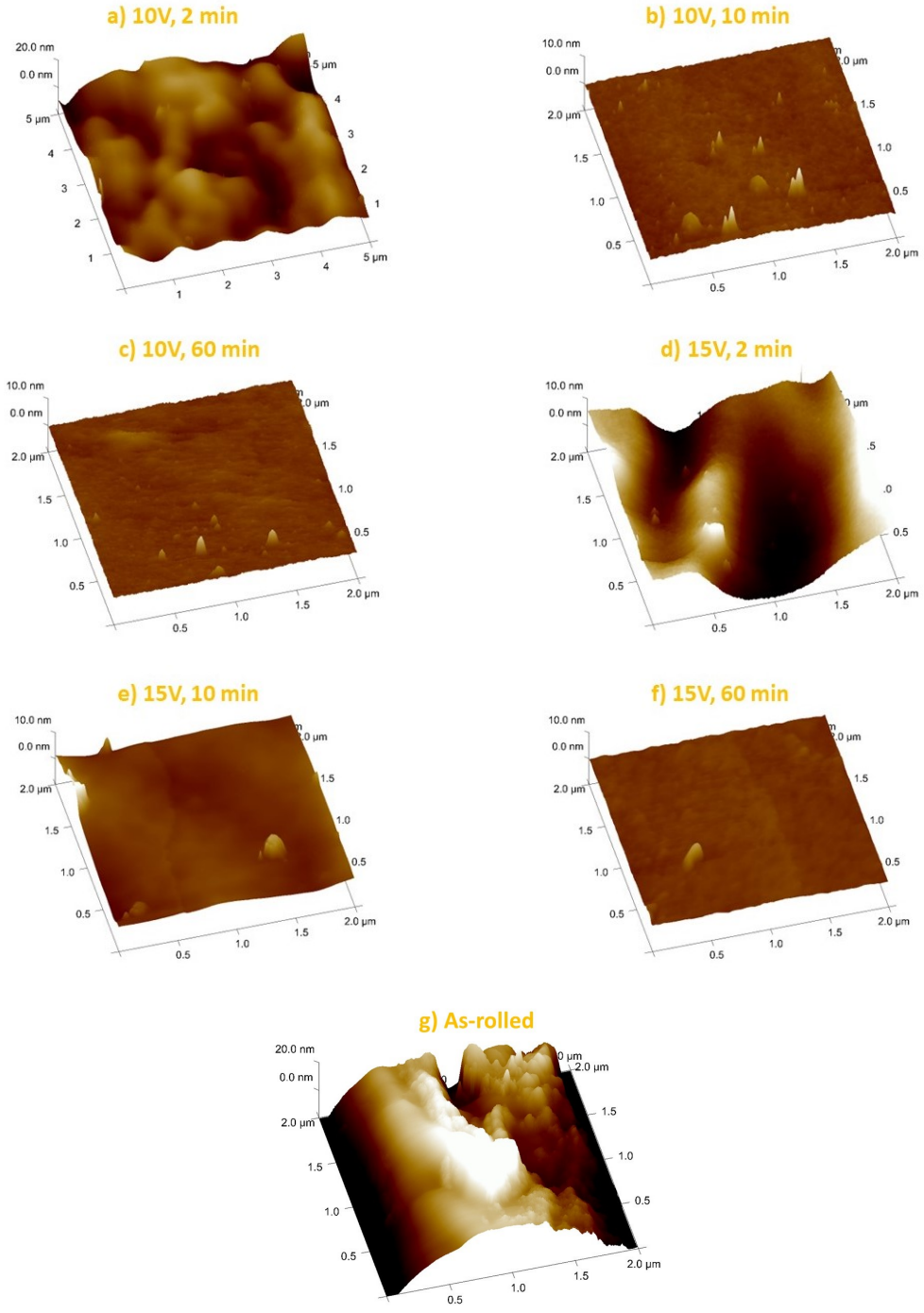

FIGURE 3.7: AFM topography of EP performed in W foil with a) 10V and 2 minutes, b) 10V and 10 minutes, c) 10V and 60 minutes, d) 15V and 2 minutes, e) 15V and 10 minutes, f) 15V, 60 minutes. g) As-rolled also added for comparison.

where N is the number of surface spots measured, z_i represents the height of the surface at each spot and $\bar{z}$ is the mean height of the surface. The values are represented in Table 3.3, as well as in Figure 3.8, along with the respective parameters of the exponential data fit. The surface roughness of the W samples decreases exponentially with the increase of EP time, a reported trend for W EP (Section 1.5.2.3). This is confirmed by the reduced Chi-square values close to unity for both fits. The initial roughness of the tungsten surface was 13.9 nm, while the lowest value obtained was for EP8 (15V, 60 minutes), with Rq= 0.375 nm. The EP setup with 10V appears to be slightly more effective in smoothing the surface.

To better understand the progression of R_q within the voltage and time ranges considered, a contour color plot was created (Figure 3.9).

Data interpolation was performed using Origin, which created a standard contour-color plot from XYZ data (X being time, Y being potential, and Z being R_q). The plot used the same potential and EP time range as before. The color scheme represents the

Sample	Potential (V)	Time (min)	R_q (nm)
AR	0	0	13.9
EP3	10	2	2.43
EP4	10	10	0.586
EP5	10	60	0.419
EP6	15	2	4.8
EP7	15	10	0.982
EP8	15	60	0.375

TABLE 3.3: R_q values obtained from the AFM images for the EP and as-rolled samples.

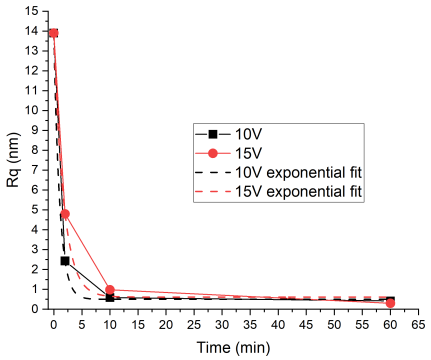

(A) R_q obtianed from AFM for EP with 10V and 15V.

Model	Exponential	
Equation	R_q = A1*exp(-t/t1) + R_{q0}	
Plot	10V	15V
R_{q0}	0,50201 ± 0,08317	0,61384 ± 0,32648
A1	13,39797 ± 0,14394	13,28203 ± 0,55593
t1	1,03171 ± 0,03823	1,73802 ± 0,19108
Reduced Chi-Sqr	0,01381	0,20508
R-Square (COD)	0,99989	0,99825
Adj. R-Square	0,99967	0,99476

(B) Exponential fit parameters for the R_q(t) graph, for 10V and 15V.

FIGURE 3.8: R_q study for EP3 (10V, 2 minutes), EP4 (10V, 10 minutes), EP5 (10V, 60 minutes), EP6 (15V, 2 minutes), EP7 (15V, 10 minutes) and EP8 (15V, 60 minutes), with the W sample without EP for reference (t=0 minutes).

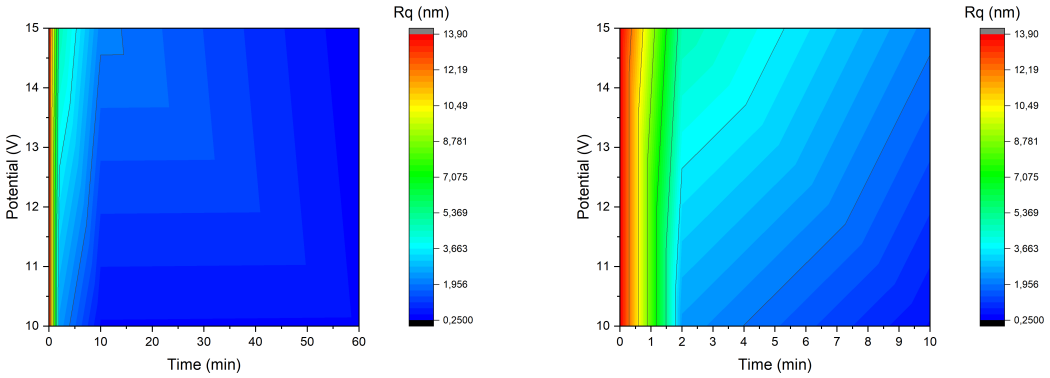

FIGURE 3.9: Contour-color plot used for interpolation of surface roughness of W EP in the potential range 10-15V and in the time range a) 0-60 minutes and b) 0-10 minutes.

R_q variation, where higher values are represented by red (warm colors) and lower values by blue (cool colors). A diagonal transition from 15V to 60 minutes is observed, with R_q decreasing. For more than 10 minutes of EP time, it has been confirmed that the R_q values are reduced. If the EP time is less than 2 minutes, the surface roughness is high, and a significant increase in R_q is observed when the EP time is decreased. Potentials within the range 13-15V reveal a smoother transition in surface roughness from 2 to 5 minutes of EP time.

3.5 Conclusions

In this chapter, different EP parameteres were explored, such as stirrer speed, electrolyte concentration, applied potential and EP time. The W polarization curve was used to determine the usable potential range for the EP, as well as to provide insight into the optimum electrolyte rotation speed value. High electrolyte rotation speeds were found to cause excessive removal of the viscous layer formed in the EP process, leading to an optimized rotation speed of 0 rpm. Electrolyte concentration revealed to strongly influence the EP outocme, with high values causing persistent anisotropic etching in the W foil, which affected the effectiveness of the EP process. Thus, 0.125M NaOH was the electrolyte chosen. Surface roughness followed an exponential decrease tendency with increasing EP time, resulting in very smooth W surfaces for high EP time values (R_q=0,375 nm for V = 15V and t = 60 minutes), and ripple-patterned, uniform surfaces for shorter ones. A 10V potential yielded a slightly better smoothing effect than the 15V potential. Additionally,

this W-smoothing analysis will be applied to the subsequent nanotube anodic growth and solar performance study, which is a novel application of W EP.

Chapter 4

Influence of Tungsten Electropolishing in the Growth of WO_3 Self-Ordered Nanotubes by Anodization

As discussed in previous chapters, highly ordered WO_3 NTs can be achieved by electrochemical anodization. NT growth quality can be quantified by measuring geometrical features, such as length (L), barrier layer thickness (δ_b), pore diameter (D_p), interpore distance (D_{int}) and porosity (P).

In this chapter, a thorough examination will be conducted to investigate the effect of W surface profile on the subsequent anodization process, which will be expressed in the geometric measurements of NT morphology mentioned above. The findings from this research will be essential for exploring the influence of W EP on the photoelectrochemical performance of anodic WO_3, a topic that has not been investigated before.

4.1 Experimental Details

Prior to anodization, the W samples described in Table 3.3 were ultrasonically cleaned in sequential 10 minutes steps in acetone, ethanol and deionized water. The anodization setup used was the one pictured in Section 2.2.3. The process was carried out under constant applied voltage (40V) for 1 h, with the electrolyte described in Section 2.1 rotating

at a speed of 100 rpm. Morphological characterization of the anodized samples was performed with Scanning Electron Microscopy (SEM). Geometrical features were measured using the software ImageJ [40].

4.2 Anodization Curves

The W samples, subjected to varying EP conditions as outlined in Table 3.3, underwent anodization at 40V for a duration of 1 hour, substantiating this study. The corresponding anodization curves are shown in Figure 4.1a, as well as their respective transient period (Figure 4.1b). The results demonstrate that oxidation and dissolution do not reach equilibrium after attaining the maximum j value, as evidenced by the exponential decay in Figure 4.1a observed in all curves. This behavior aligns with previous reports for W [104, 105] and other metals, such as Ti [106]. For all the W samples with EP, the behavior of $j(t)$ remained consistent until reaching 20 minutes of anodization, displaying a plateau after this time (Figure 4.1a). In fact, in the case of ZrO_2 NT growth by anodization, a change in the $j(t)$ trend was identified, expressed in a steep drop in current density after 3 minutes of anodization time at 80V in a fluoride-containing electrolyte [107]. This revealed that a new nucleation phase was initiating, resulting in the formation of a second layer of NTs on top of the first. Although, it appears that a new stage with a behavior similar to the reported case has emerged here, as, after 20 minutes, a stabilization of j(t) has been achieved, in contrast to the previously reported case. The transient period depicted in Figure 4.1b exhibits the characteristic stages of self-ordered nanoporous formation (Figure 1.5), indicating the successful achievement of self-ordered nanopores or nanotubes in all samples. However, the as-rolled sample (red dots in Figure 4.1b) exhibits a more pronounced shoulder-like trend after j_{max} is achieved, a characteristic of the anodization process [106]. This evidences that the competition for NT growth is more intense without the W EP surface treatment, which confirms that the W EP process improves the growth of WO_3 self-ordered NTs.

Examining the curves in 4.1b more closely, the minimum and maximum values of the current density in the transient period can be identified, labeled as j_{min} and j_{max} respectively, as well as the time values at which they occur, t_{min} and t_{max}. In order to gain a deeper understanding of the data, Figures 4.2 and 4.3 display the values of $\Delta t = t_{max} - t_{min}$ and $\Delta j = j_{max} - j_{min}$ for all curves, as well as the quantities mentioned above.

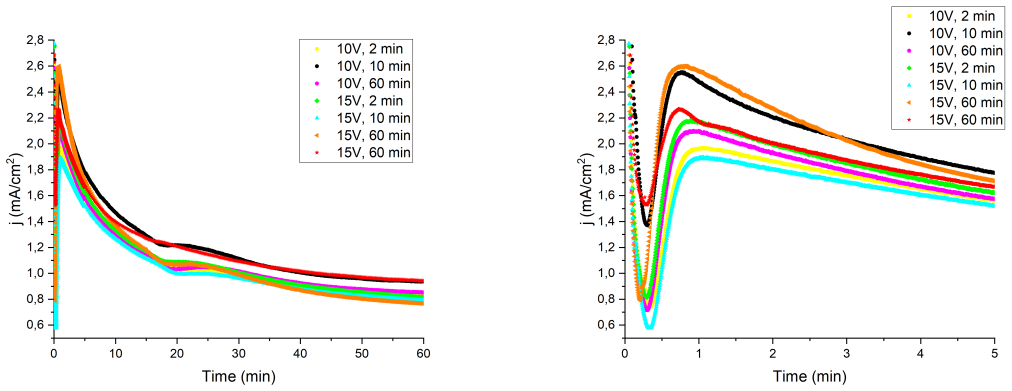

(A) (B)

FIGURE 4.1: a) Anodization curves obtained for the EP and as-rolled W samples and b) their respective transient period.

Apart from the sample with an EP with 10V and 10 minutes, all EP samples reveal a longer nucleation time than the as-rolled one, as is evidenced by the longer Δt values in Figure 4.2. The samples with the longest nucleation time are the EP with 10V, 2 minutes and 15V, 10 minutes, while the shortest Δt are seen in the as-rolled and the EP with 10V, 10 minutes. The graph in Figure 4.3 demonstrates that the change in Δj is consistent regardless of the EP potential as the EP time progresses. The W samples with EP reveal higher Δj, while the sample with EP with 10V, 10 minutes had the lowest Δj and the highest j_{min} of them all. This suggests that the W samples without surface treatment and with an EP with 10V, 10 minutes produced NTs with the lowest dissolution rate during the nucleation phase, which is in agreement with the low Δt values reported.

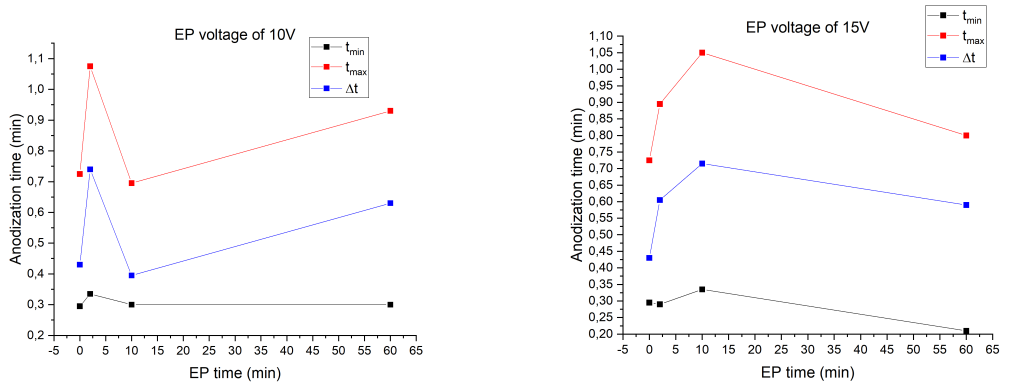

(A) (B)

FIGURE 4.2: t_{min}, t_{max} and $\Delta t = t_{max} - t_{min}$ evolution with EP time for anodized W samples with EP voltage of a) 10V and b) 15V.

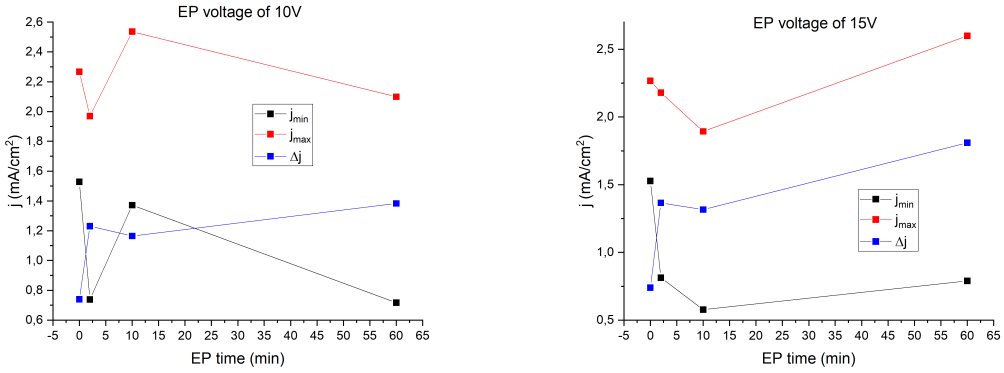

(A) (B)

FIGURE 4.3: j_{min}, j_{max} and $\Delta j = j_{max} - j_{min}$ evolution with EP time for anodized W samples with EP voltage of a) 10V and b) 15V.

The evolution of charge over time during the synthesis ($Q(t)$) is obtained by integrating $j(t)$ (equation 4.1):

$$Q(t) = \int j(t)dt \tag{4.1}$$

Figure 4.4 reveals that the anodization of WO_3 is not a steady-state process, as evidenced by the non-linear evolution of the curves Q(t), in agreement with the findings in the anodization curves. This is due to the non-balance between oxidation and dissolution processes, where the oxidation rate is higher than the dissolution, typical in some valve metals [106] and already reported for W anodization [40]. The W samples without EP and the one with 10V and 10 minutes demonstrate a higher total charge transferred in the anodization process than the other samples, indicating a slower oxidation rate.

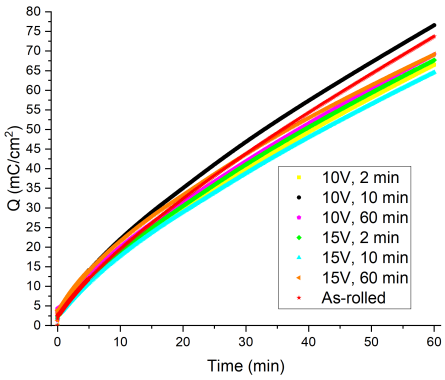

FIGURE 4.4: Charge evolution during the anodization process for the anodized EP and as-rolled samples.

4.3 Morphological Analysis

The SEM images in Figure 4.5 present a top-view of the anodized EP W samples and of the sample without EP. The WO_3 NTs obtained from the anodization of the as-rolled sample demonstrate a considerable degree of desegregation, appearing to be a fragile thin layer. Similar observations are detected for samples obtained from EP with 10V, 10 minutes, 15V, 60 minutes and 10V, 60 minutes, however with less desegregation and a thicker nanoporous layer. On the other hand, W samples submitted to an EP with 10V, 2 minutes, 15V, 2 minutes and 15V, 10 minutes produced organized, self-ordered NT arrays.

SEM cross-sectional images support the aforementioned top-view observations, revealing that W samples exhibit distinct morphological characteristics that can be categorized into two groups: the anodized W samples that reveal self-ordered NT growth along the entire anodization time (EP with 10V and 2 minutes, 15V and 2 minutes and 15V and

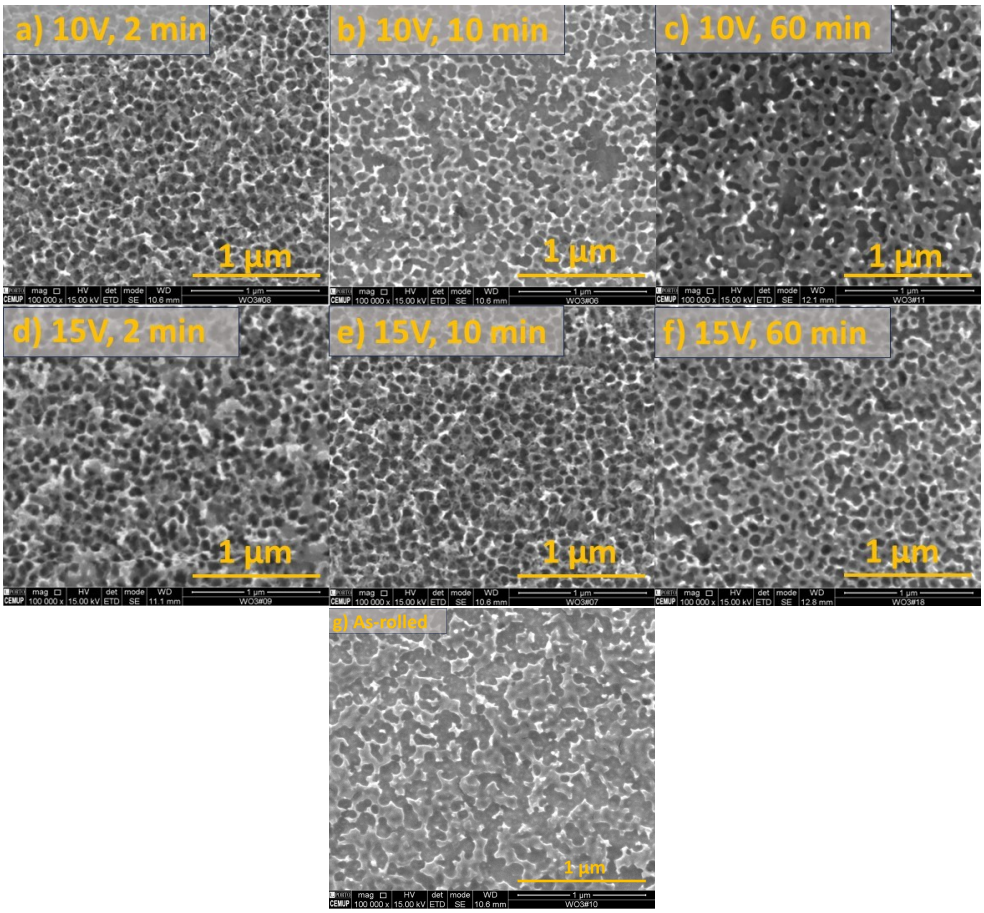

FIGURE 4.5: SEM top-view morphology images of WO_3 NTs grown by anodization in W foil submitted to EP with a) 10V and 2 minutes, b) 10V and 10 minutes, c) 10V and 60 minutes, d) 15V and 2 minutes, e) 15V and 10 minutes, f) 15V, 60 minutes. Anodization of g) as-rolled W sample (without EP) added for comparison.

10 minutes - group 1) and the samples that demonstrate a dense oxide layer formed underneath a desegregated thin nanoporous top layer created during the initial stages of anodization transient period (EP with 10V, 10 minutes, 10V, 60 minutes, and 15V, 60 minutes and W sample without EP - group 2). It appears that the oxidation-dissolution ratio was interrupted for samples from group 2. As mentioned in the anodization curves analysis, a current density plateau was identified at 20 minutes for all samples, meaning that an equilibrium between oxidation and dissolution rates was achieved. Thus, we believe that this phenomenon is linked with the transition from self-ordered NT growth to dense oxide film formation in samples from group 2.

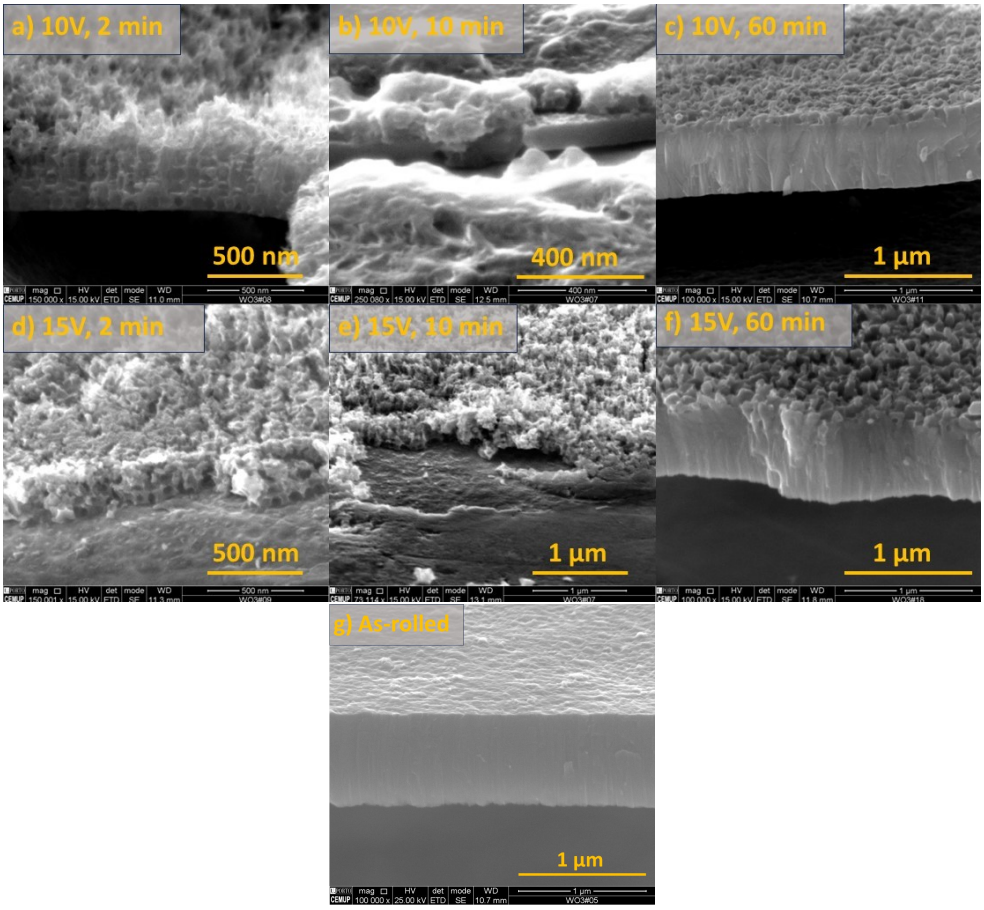

FIGURE 4.6: SEM cross-sectional morphology images of WO_3 NTs grown by anodization in W foil submitted to EP with a) 10V and 2 minutes, b) 10V and 10 minutes, c) 10V and 60 minutes, d) 15V and 2 minutes, e) 15V and 10 minutes, f) 15V, 60 minutes. Anodization of g) as-rolled (without EP) also added.

Group 1	Group 2
10V, 2 minutes	10V, 10 minutes
15V, 2 minutes	10V, 60 minutes
15V, 10 minutes	15V, 60 minutes
	As-rolled

TABLE 4.1: Groups of W EP samples identified by their respective surface treatment. Group selection is based on their subsequent WO_3 morphological outcome.

4.4 Geometrical Features

4.4.1 Porosity Analysis

Pore diameter (D_p) and inter-pore distance (D_{int}) were estimated from the SEM top-view images in Figure 4.5, defined as described in Figure 4.7.

To qualitatively analyse the ordering degree of self-organised arrays of NPs, porosity (P) is calculated from equation 4.2 [108] for each sample:

$$P = \frac{2\pi}{\sqrt{3}} \left(\frac{D_p}{2D_{int}} \right) \tag{4.2}$$

These quantities are presented in Table 4.2. D_p shows similar measurements for all samples, with a mean value of 56 nm. The anodized as-rolled sample porosity follows the 10% rule established for alumina NPs [108]. Regarding the anodized W samples with an EP, a much higher porosity was obtained, with an average value (30.4%) that is 179% greater than the porosity of the W sample that was not subjected to surface treatment (10.9%). The W samples that produced a desegregated, thin nanoporous layer on top of a dense, nonporous oxide (group 2 - Section 4.3) reveal porosity values lower than 23%, while also showing a high standard deviation in the D_{int} measurements. On the other hand, samples that were able to form self-ordered NT arrays showed porosity values

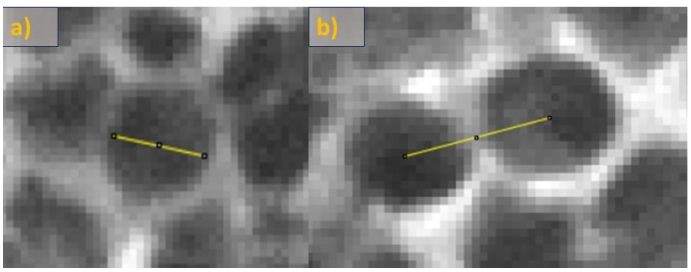

FIGURE 4.7: a) D_p measurement defined as the pore diameter and b) D_{int} defined as the distance between the center of two adjacent pores. Images are zoomed-in areas of the SEM top-view images in Figure 4.5.

	EP	D_p (nm)	D_{int} (nm)	P (%)
Group 1	10V, 2 minutes	62 ± 11	86 ± 11	46.2
	15V, 2 minutes	58 ± 13	94 ± 13	34.4
	15V, 10 minutes	64 ± 10	92 ± 11	44
Group 2	As-rolled	64 ± 10	186 ± 78	10.9
	10V, 10 minutes	41 ± 11	110 ± 50	12.5
	10V, 60 minutes	53 ± 12	106 ± 21	22.8
	15V, 60 minutes	51 ± 9	101 ± 24	22.7

TABLE 4.2: D_p, D_{int} and P of the anodized EP and as-rolled samples, split according to their morphological group (Table 4.1).

ranging from 34% to 47% (group 1). This indicates a high pore density, which is in agreement with the balanced oxidation and dissolution rates observed during the anodization of these samples.

4.4.2 Anodic WO_3 Oxide Length Analysis

Following the distinct morphological behavior reported for the anodized W samples, different oxide lengths will be defined and measured from the cross-sectional images in Figure 4.6: L_Q (estimation of the NT length - all groups of samples), L_{SEM} (total oxide length obtained regardless of the morphological typology - all groups), L_{NT} (NT length for the samples that produced a thick oxide - group 2) and L_{oxide} (thick oxide film length - group 2). Adapting the Faraday's law of electrolysis [94], L_Q can be calculated from equation 4.3:

$$L_Q = \frac{QM}{Fn\rho} \tag{4.3}$$

where Q (C.cm^{-2}) is the total charge flow during synthesis (Figure 4.4), M = 231.84 g.mol^{-1} is the molecular weight of WO_3, F = 96500 C.mol^{-1} is the Faraday constant, n = 6 is the number of electrons involved in the oxidation reaction and ρ = 7.16 g.cm^{-3} is the density of WO_3.

Table 4.3 compares the obtained L_Q and L_{SEM} for all anodized W samples. Regardless of the EP potential and time, L_Q is $\sim$ 400 nm, in agreement with previous reports for WO_3 fabricated by anodization [40]. A considerable difference between L_Q and L_{SEM} is observed for samples from group 2, which is expected as these anodizations were found to be unbalanced, resulting in the formation of a thick oxide film. On the other hand, samples from group 1 reveal to achieve NT lengths similar to the estimated values.

	EP	L_Q (nm)	L_{SEM} (nm)
Group 1	10V, 2 minutes	372	398 ± 30
	15V, 2 minutes	378	316 ± 48
	15V, 10 minutes	361	348 ± 27
Group 2	As-rolled	414	709 ± 7
	10V, 10 minutes	428	220 ± 12
	10V, 60 minutes	387	684 ± 52
	15V, 60 minutes	387	658 ± 34

TABLE 4.3: Anodized EP samples separated by their morphological groups defined in Table 4.1, with the respective NT length estimation (L_Q) and oxide length SEM measurement (L_{SEM}).

4.4.2.1 Oxide Length Study in Samples that Produced a Nonporous Oxide

A link was established between the thick oxide film formation and the anodization $j(t)$ plateau at 20 minutes for samples from group 2 (Table 4.1). Thus, a comparative study was conducted between the L_Q values at 20 minutes of anodization and L_{NT} for the EP samples from group 2 (Table 4.1), as shown in Table 4.4. Additionally, the obtained R_q values for these EP samples and L_{oxide} are also reported.

In fact, L_{NT} is consistent with the estimated L_Q at 20 minutes, which confirms that, after this time, the oxide began to grow as a dense film. Therefore, the current plateau is confirmed to have an impact on the normal growth of NTs for these samples.

As seen in Table 4.4, the R_q values are identically low for all samples. Moreover, the analysis of these EP samples from Section 3.4 revealed that very smooth surfaces were attained. Thus, these W surfaces were profiled without nucleation sites prior to anodization. Given this, a connection between these findings and anion incorporation into the oxide layer can be established. It has been proposed that anions may have an effect on the oxide layer during the anodization process [109]. This theory states that an anion-contaminated layer forms on top of the oxide barrier after δ_b^{max} is reached. The greater the thickness of this layer, the more probable it is for NTs to form, whereas a thinner layer increases the likelihood of a dense oxide film being produced [110]. Thus, we believe that the nanoporous layer formed initially nucleated poorly as a consequence of the absence of nucleation sites in these samples, leading to surface defects on the oxide surface in contact with the electrolyte after reaching δ_b^{max}. Considering that the electric field is more concentrated in depressed sites (see Section 1.4.2), the accumulation of F^- in the oxide surface could have been difficult in these samples at 20 minutes, facilitating the growth of the nonporous oxide film. The anodized sample with a prior EP with 10V and 10 minutes

EP	L_Q (nm)	L_{NT} (nm)	L_{oxide} (nm)	R_q (nm)
10V, 10 minutes	161.2	139 ± 12	80.7 ± 0.7	0.586
10V, 60 minutes	167.6	128 ± 23	556 ± 46	0.419
15V, 60 minutes	174.9	161 ± 31	497 ± 13	0.375

TABLE 4.4: Relation between L_{NT} and L_Q at the time when the current plateau started in the EP anodization curves for the EP samples from group 2 (Table 4.1). L_{oxide} and R_q of the EP samples added for further analysis.

reveals the shortest oxide film formed (L_{oxide} = 80.7 ± 0.7 nm), which is consistent with the highest Q obtained for this sample in the anodization curves analysis. These findings also apply to the as-rolled W sample, as despite showing a different R_q from these EP samples (13.9 nm), the analysis in Section 3.4 revealed a non-uniform surface profile, which also affects the NT growth quality.

Regarding the samples from group 1 in Table 4.5, the R_q values are similar and higher than those of samples from group 2, evidencing dimple-like, uniform-shaped W surfaces prior to anodization (Section 3.4). Therefore, this surface profile positively impacts the subsequent growth of WO_3 NT by anodization, with the EP sample with 10V and 2 minutes revealing the largest NT length (L_{SEM} = 398 ± 30 nm). The dimple surface pattern was reported to be used to obtain highly ordered NT arrays in other metals, such as Al [102, 111].

4.4.3 Oxide Barrier Layer Thickness Analysis

To finalize this analysis, Table 4.6 compares the final oxide layer thickness values obtained from the SEM cross-sectional images (δ_b^{SEM}) and from equation 1.5 (δ_b) for the EP samples that grew self-ordered NT arrays (group 1). Here, δ_b^{SEM} was measured as described in Figure 4.8, which shows similar values across all samples consistent with δ_b. Given that δ_b is theoretically dependent on the anodization potential [40], these results are expected, as the applied anodization potential for these experiments was constant (40V). The sample submitted to an EP with 10V, 2 minutes demonstrated the strongest correlation between

EP	L_Q (nm)	L_{SEM} (nm)	R_q (nm)
10V, 2 minutes	372	398 ± 30	2.43
15V, 2 minutes	378	316 ± 48	4.8
15V, 10 minutes	361	348 ± 27	0.982

TABLE 4.5: L_Q, L_{SEM} and R_q for the anodized EP samples from group 1 (Table 4.1).

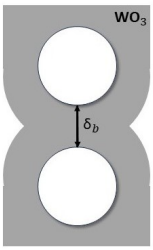

FIGURE 4.8: Schematic representation of the δ_b^{SEM} measurement, defined as the distance between two vertical holes inside a WO_3 NT.

EP	δ_b (nm)	δ_b^{SEM} (nm)
10V, 2 minutes	56.94	56 ± 6
15V, 2 minutes	56.98	48 ± 4
15V, 10 minutes	57.06	48 ± 7

TABLE 4.6: δ_b^{SEM} and δ_b for the anodized samples from group 1 (Table 4.1).

the two values, while also revealing the highest final oxide thickness obtained. The values are in agreement with a previously reported estimation model for δ_b for anodic WO_3 [40].

4.5 As-rolled Sample Analysis

The electrolyte rotation parameter was set at 100 rpm for all anodizations. However, given the odd results obtained for the as-rolled sample, a study comparing electrolyte rotations was developed. Figure 4.9 illustrates the top-view SEM images obtained for the as-rolled samples with electrolyte rotations of 100 rpm and 60 rpm. The sample grown with 60 rpm reveals a more organized nanotemplate structure, confirmed by D_p = (61 $\pm$ 8) nm, D_{int} = (105 $\pm$ 45) nm and P = 30.4%. This represents a 79% porosity improvement for the 60 rpm anodization.

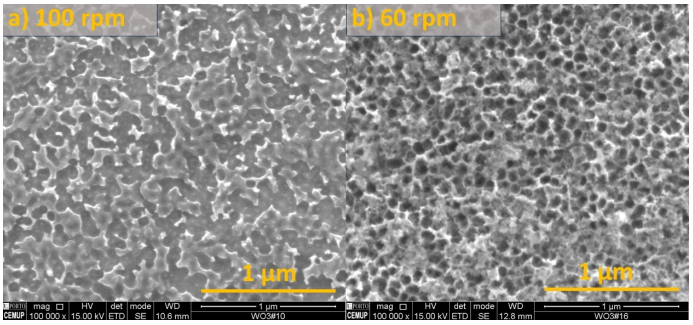

FIGURE 4.9: SEM top-view images of anodized W as-rolled samples with an electrolyte rotation speed of a) 100 rpm and b) 60 rpm.

4.6 Conclusions

In this work, WO_3 NTs were grown by electrochemical anodization. The EP process was found to decrease pore competition during the nucleation phase, allowing a more effective NT vertical growth. Moreover, increased porosity and pore dimensions when compared to the as-rolled reference were verified as well for the EP samples, resulting in a 179% mean porosity improvement. The W EP samples revealing low R_q (<1nm) or high R_q with non-uniform profiles developed a thick, dense oxide film beneath a nanoporous template. On the other hand, EP samples that exhibited uniform ripple-like surfaces with R_q values wihtin the range 1-5 nm produced NTs with the highest porosity and NT length. The anodization performed in the EP sample with 10V and 2 minutes revealed the highest porosity (46.2%) and longest L_q (398 ± 30 nm), as well as a barrier oxide layer similar to the expected value (56 ± 6 nm). Regarding the as-rolled analysis, an electrolyte rotation speed of 60 rpm was found to be beneficial for the anodization process, increasing porosity values by 79%.

Chapter 5

Annealing Optimization in Anodic WO_3 Self-Ordered Nanotubes for Solar Water Splitting

The WO_3 NTs produced through anodization are not suitable for PEC applications in their amorphous state. To obtain crystallinity, they must be thermally treated, resulting in a rearrangement of their structure. This chapter will explore the thermal annealing optimization of W as-rolled anodized samples, as previous research on anodic WO_3 has not been able to come to an agreement on the best annealing parameters for the material, as the nanostructure collapse reports for some annealing conditions indicate [40, 58]. The optimized annealing conditions, when combined with the optimized W EP parameters from previous chapters, will be used to investigate the effect on the photoelectrochemical performance of anodic WO_3, a new application of this research.

5.1 Experimental Details

As-rolled W samples were anodized prior to thermal annealing for 1h at 40V and with an electrolyte rotation speed of 60 rpm (the other setup conditions are detailed in Section 2.2.3). The procedure involves gradually increasing the temperature of the sample according to a predetermined heating ramp until the desired annealing temperature is attained. This temperature is then kept for two hours, before the process is completed with a gradual cooling at 8ºC/min, until the temperature returns to ambient. Each sample was subjected to a different annealing condition (Table 5.1): 500°C with a 1°C/min heating

Sample	Temperature (ºC)	Heating ramp (ºC/min)
A1	500	1
A2	500	2
A3	600	1

TABLE 5.1: Annealing conditions considered for the annealing optimization study in the anodized as-rolled W samples.

rate, 500°C with a 2°C/min heating rate [40, 58], and 600°C [58] with a 1°C/min heating rate. Morphological analysis was performed with SEM. Structural characterization was conducted with X-Ray Diffraction (XRD).

5.2 Morphological Characterization

Figure 5.1 depicts the SEM top-view images of the anodized samples after thermal annealing, as well as one without thermal treatment for comparison. The cross-sectional images of the thermal annealed samples are also presented in Figure 5.2 to gain a better understanding of the structural impact caused by the treatment.

Annealing reveals to change the samples anodized layer morphology, with the thermal treatment under 500ºC, 1ºC/min and 500ºC, 2ºC/min transitioning from a nanoporous layer into a nanoparticle-like structure, as previously reported in [40]. However, the sample heated to 500ºC at a rate of 2ºC/min appears to be slightly more dispersed, evidenced in Figure 5.1. A dense oxide layer underneath the nanoporous structure is formed in these annealings, as seen in Figure 5.2 and predicted for this temperature (Section 1.4.3). The formation of this oxide layer is attributed to the thermal oxidation of the underlying W foil during the annealing process [57]. The nanoporous layer appears to have been more affected in the 500ºC, 2ºC/min annealing, as the lower structure length in Figure 5.2 evidences. Regarding the thermal annealing under 600ºC, 1ºC/min, a nanoporous structure collapse is observed, confirming that the slower heating ramp does not alter the expected result for a thermal treatment with 600ºC (Section 1.4.3). As seen in Figure 5.2, the nanoporous layer is no longer visible and the largest compact oxide length is observed, indicating that the NTs have completely disintegrated, which is consistent with the structure collapse reports for this temperature (Section 1.4.3).

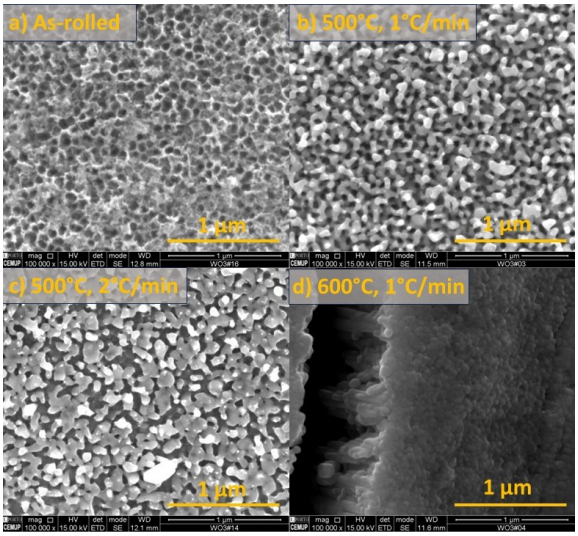

FIGURE 5.1: SEM top-view images of anodized W as-rolled samples a) without thermal treatment and after thermal annealing with b) 500ºC, 1ºC/min, c) 500ºC, 2ºC/min and d) 600ºC, 1ºC/min.

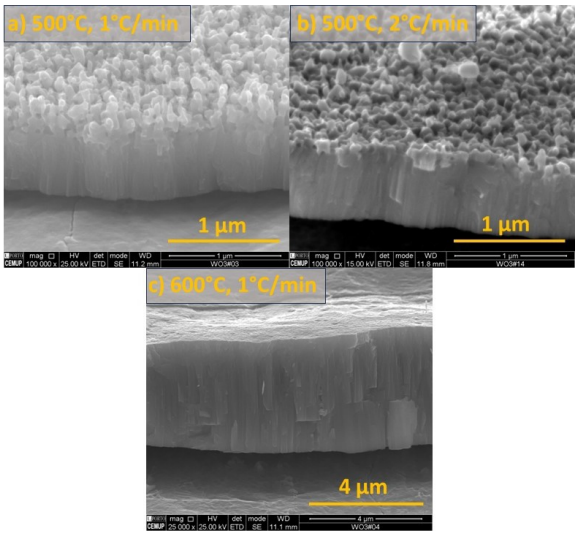

FIGURE 5.2: SEM cross-sectional images of anodized W as-rolled samples after thermal annealing with a) 500ºC, 1ºC/min, b) 500ºC, 2ºC/min and c) 600ºC, 1ºC/min.

5.3 Structural Characterization

The XRD patterns of the WO_3 NTs for the annealed and as-anodized samples, as well as the W foil data, are shown in Figure 5.3. These patterns were obtained using Bragg-Brentano focusing geometry.

The thermal annealed samples reveal intensity peaks characteristic of the WO_3 monoclinic phase, corresponding to the (002), (020), (220), (022), (220), (004) and (040) planes

(JCPDS 01-083-0950). The as-anodized W sample confirms the amorphous structure assumption, as the only intensity peaks shown are those corresponding to the W characteristic planes [(110), (200), (211)]. In the case of the W diffractogram, some WO_3 monoclinic phase peaks are visible between 2θ=20° and 2θ=30° in Figure 5.3. This occurs because the W surface chosen to perform XRD analysis was part of the sample submitted to thermal annealing with 500°C, 1°C/min, which enabled the detection of these peaks on the metal surface.

Figure 5.4 illustrates the magnified spectra at the reference peaks of the monoclinic phase triplet, corresponding to the crystallographic planes (002), (020) and (200). The curves of all annealed samples show a wide, broad main peak, which is a result of the convolution of the first two peaks related to the [002] and [020] Bragg directions. These samples also showed preferential growth in the [020] direction, as evidenced by the most intense peak at 2θ = 23,39° for 500°C, 1°C/min, 2θ = 23,41° for 500°C, 2°C/min and 2θ = 23,36° for 600°C, 1°C/min. The [002] growth direction of monoclinic WO_3 has been demonstrated to result in improved PEC performance for water oxidation, with lower

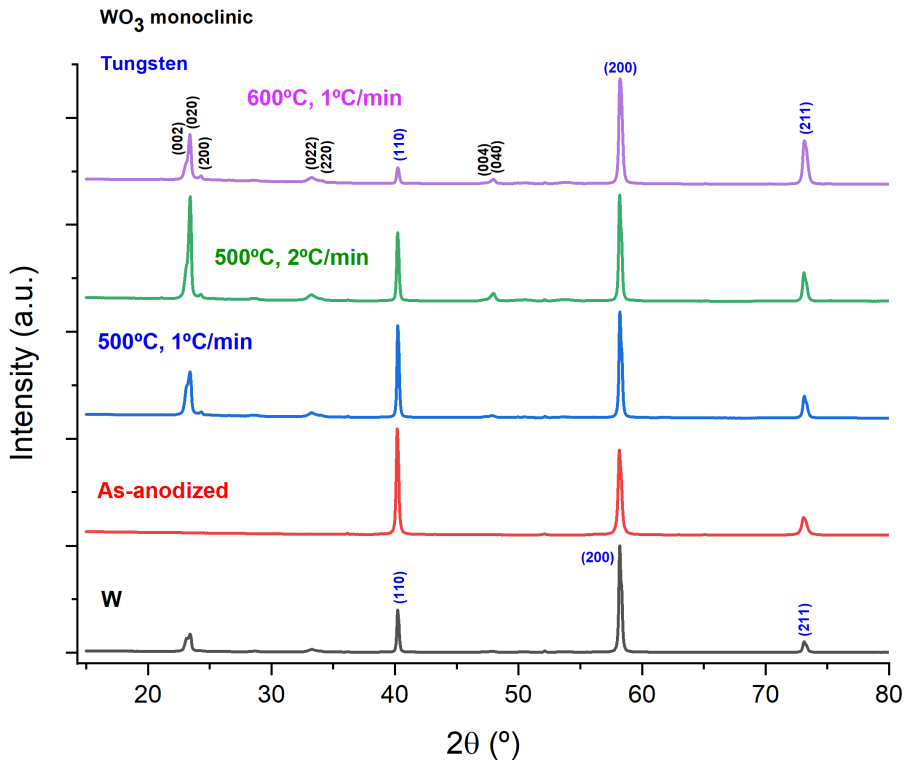

FIGURE 5.3: XRD patterns of W foil, as-anodized W sample without thermal treatment and after thermal annealing with 500°C, 1°C/min, 500°C, 2°C/min and 600°C, 1°C/min.

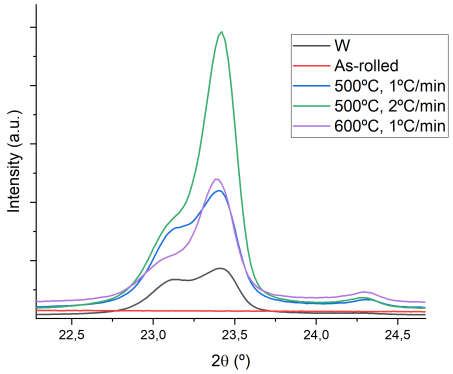

FIGURE 5.4: Magnified XRD patterns at the reference peaks of the monoclinic phase triplet of the WO_3 in the W foil, the as-anodized W sample without thermal treatment and after thermal annealing with 500ºC, 1ºC/min, 500ºC, 2ºC/min and 600ºC, 1ºC/min.

overpotentials than other orientations [40, 112]. Thus, it might indicate that the annealed sample with 500ºC, 2ºC/min reveals the best photoperformance.

The average crystal size (D) can be calculated using Scherrer's equation:

$$D = \frac{k\lambda}{w \cos\theta} \tag{5.1}$$

where w is the full width at half maximum (FWHM) intensity, k is a constant (0.94), and λ is the incident X-ray wavelength (1.56056 $\AA$) [51]. Using equation 5.2, the volume of the unit cell (V) was obtained:

$$V = a \cdot b \cdot c \cdot \sin\beta \tag{5.2}$$

where a, b and c are the lattice constants of the monoclinic structure and β = 90.89º is the angle between a and c. These quantities were extracted by applying a Pseudo-Voigt fit to the XRD data (Appendix A).

The thermal annealing with 500°C, 1°C/min yields an average crystal size that is slightly higher than the results of the other treatment conditions, yet the monoclinic unit

Annealing	a ($\AA$)	b ($\AA$)	c ($\AA$)	D (nm)	V ($\AA^3$)
500ºC, 1ºC/min	7.3145	7.6013	7.6968	45.35	427.89
500ºC, 2ºC/min	7.3264	7.5928	7.6843	42.4	427.41
600ºC, 1ºC/min	7.3204	7.6102	7.6707	42.75	427.33

TABLE 5.2: Lattice parameters (a, b, c), average crystal size (D) and monoclinic unit cell volume (V) of the WO3 NPs after thermal annealing with 500ºC, 1ºC/min, 500ºC, 2ºC/min and 600ºC, 1ºC/min.

cell is similar across all procedures. All parameters are comparable to the typical values of WO_3 monoclinic (a = 7.3008 $\AA$, b = 7.5389 $\AA$, c = 7.6896 $\AA$, V = 423.19 $\AA^3$ JCPDS 01-083-0950).

5.4 Conclusions

This study investigated the optimization of the annealing of WO_3 NTs. A dense oxide film was created beneath the nanoporous layer when the thermal annealing was conducted at 500ºC. However, when the temperature was increased to 600ºC, the nanoporous structure collapsed. Crystallographic planes associated with the monoclinic phase of WO_3 were observed in all annealed samples, with the best photoperformance being achieved when annealing was performed at 500°C with a heating rate of 2ºC/min. The lattice constants, average crystal size, and unit cell volume were determined and were found to be within the typical range of values for monoclinic WO_3. Further PEC characterization is now achievable by applying the optimized annealing and EP conditions to the fabrication of anodic WO_3 NTs.

Chapter 6

Photoelectrochemical Characterization of Anodic WO_3 Fabricated with Optimized Annealing and Electropolishing Conditions

This thesis work is finalized with the assessment of the photoelectrochemical performance of anodic WO_3 produced with the previously optimized EP and annealing parameters.

6.1 Experimental Details

W samples were anodized for 1h at 40V with an electrolyte rotation speed of 60 rpm (the other setup conditions are detailed in Section 2.2.3). Two anodic WO_3 samples were fabricated: one from an as-rolled W sample and another from a W sample treated with EP with 10V and 2 minutes. Both samples were then submitted to thermal annealing at 500ºC for 2h, with a heating ramp of 2ºC/min (Table 6.1). Photoelectrochemical characterization was carried out in the setup described in Section 2.3.4, obtaining the photocurrent density-voltage curves (J-V) under dark and 1 sun simulated sunlight (AM 1.5G illumination 100 $mW.cm^{-2}$).

Sample	EP	Annealing Temperature (°C)	Heating ramp (°C/min)
P1	10V, 2 minutes	500	2
P2	—	500	2

TABLE 6.1: W sample conditions for the PEC characterization study.

6.2 Photoelectrochemical Characterization

The graph in Figure 6.1 displays the photocurrent density-voltage characteristics of anodic WO_3 for both as-rolled and EP (10V, 2 minutes) W samples that have been anodized at 40V for 1h and thermally annealed at 500°C with 2°C/min of heating ramp.

Under illumination, the EP sample reveals a photocurrent density of 143 μA.cm^{-2} at 1.45 V_{RHE}, which is 5% higher than the one obtained for the as-rolled sample (136 μA.cm^{-2} at 1.45 V_{RHE}). This result confirms that a slight increase in PEC performance is verified in a smooth and uniform dimple-patterned W surface. The average crystal size appears to have an effect on the photoresponse of anodic WO_3. Despite the values obtained being in line with those reported recently (140 μA.cm^{-2} at 1 V vs Ag / AgCl [54] and 0.19 mA.cm^{-2} at 1.45 V_{RHE} [40]), a smaller crystal size (34.87 nm [40]) was reported compared to the previously calculated one (42.4 nm) for the same anodization and annealing conditions.

Regarding the onset potential, the as-rolled sample and the W sample with EP reveal similar values (~0.4 V and ~0.48 V, respectively), meaning that similar potential is required to initiate the water splitting reaction.

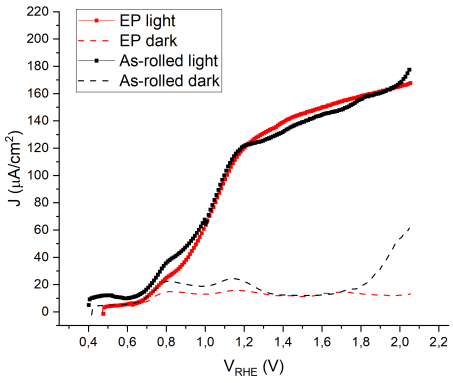

FIGURE 6.1: Photocurrent density-voltage characteristics of anodic WO_3 fabricated through anodization for W as-rolled and EP samples.

6.3 Conclusions

The effect of W EP on the photoelectrochemical performance of anodic WO_3 was studied. EP was found to enhance the photocurrent density by 5% compared to the sample without surface treatment due to the presence of nculeation sites on the W surface prior to the anodization process. The onset potential was similar for for both metallic surface profiles.

Chapter 7

General Conclusions and Future Perspectives

This thesis explored the impact of W EP and thermal annealing on the performance of WO_3 photoanodes for solar water splitting, produced by electrochemical anodization of W. There has been a scarcity of studies on the application of optimized W EP parameters for the fabrication of nanostructured WO_3 by electrochemical anodization, which is one of the focus of this research.

Firstly, an optimization study of W EP was conducted, examining the electrolyte rotation speed and concentration, applied potential, and time as the variables. The polarization curve of W was assessed, allowing the recognition of the current plateau phase and the potential range that could be used in the investigation. High electrolyte rotation speeds were found to cause excessive removal of the viscous layer formed in the EP process, and so the optimized rotation speed was 0 rpm. It was determined that the 0.5M NaOH electrolyte caused persistent anisotropic etching in the tungsten foil, which hindered the effectiveness of the EP process. Therefore, 0.125M NaOH was the electrolyte chosen. A reported trend of exponential decrease in surface roughness with increasing EP time was detected, while dimple-like, uniform W surfaces were formed for shorter EP times and smooth surfaces for longer ones. The 10V applied potential exhibited a slightly better smoothing effect than that of 15V.

Using the established ideal W EP conditions, the effects of this surface treatment in the self-ordered NT growth of WO_3 by electrochemical anodization were analysed. Anodization was performed under constant applied potential of 40V for 1h in aqueous electrolyte containing 1M Na_2SO_4 and 0.5 wt% NH_4F rotating at 100 rpm. The EP process was found

to decrease pore competition during the nucleation phase, allowing a more effective NT vertical growth. An increase in porosity was obtained for the anodized samples submitted to prior EP compared to the W sample without surface treatment. W samples with either very smooth surfaces or surfaces with high roughness and non-uniform profiles developed a dense, thick WO_3 film beneath a nanoporous template. In contrast to this, uniform, dimple-patterned W surfaces with R_q varying between 1-5 nm produced organized NT arrays. The EP sample exhibiting the highest porosity and NT length values (46.2% and 398 nm, respectively) was the one submitted to EP with 10V of applied potential and 2 minutes of EP time. Additionally, a 79% increase in porosity was registered for the anodization of W without prior EP when the electrolyte rotated at 60 rpm instead of 100 rpm.

Following the fabrication of nanostructured WO_3 through anodization, thermal annealing was used to induce crystallization. An optimization study is conducted, considering the annealing temperature and heating ramp as variables. A thick oxide film was formed beneath the nanoporous layer when the annealing temperature was set to 500ºC. However, when this temperature was raised to 600ºC, the nanoporous structure disintegrated. XRD analysis revealed the presence of crystallographic planes related to the monoclinic phase of WO_3 in all annealed samples, and also provided insight into the expected best annealing conditions for enhanced photoperformance (500°C and a heating ramp of 2°C/min).

Finally, the optimized W EP and annealing parameters were employed to create nanostructured WO_3 and assess their capability to enhance photoperformance. The ideal W EP produced WO_3 NTs that revealed a photocurrent density value of 143 μA.cm^{-2} at 1.45 V_{RHE}, a 5% increase when compared to the W sample without surface treatment. The onset potential was similar for the W sample without EP and the EP one, indicating similar potential requirements to initiate the water splitting reaction.

7.1 Future Perspectives

In this thesis work, important and innovative research was performed. However, there were some challenges faced that may require different approaches in future works related to the subject.

In the long term, new optimization studies for W EP need to be assessed. The work shown in this thesis provides a starting point for further research, however some parameters were set constant throughout the process that may be adjusted depending on the application purpose. The W sample region in contact with the electrolyte was adjusted to meet the requirements of the photoelectrochemical characterization device, and altering it produces entirely different outcomes. Thus, altering the W surface area submitted to EP implies the need of a new comprehensive study regarding the remaining EP conditions.

The current density plateau reported for the W anodization curves at around 20 minutes is a phenomena never explained before. This current levelling appears in all curves, however, depending on the prior W surface profile, only in some cases does it actually reveal to influence the normal WO_3 NT growth. Given this, it is suggested further investigation regarding this topic not only to confirm this thesis findings but also to fully understand the mechanisms that lead to such occurrence. Additionally, it is recommended to conduct a thorough investigation of the effect of W EP on the development of WO_3 NTs when the anodization electrolyte is rotated at 60 rpm, due to the increased porosity observed in the anodization process at this speed.

Further investigation into the annealing process may be conducted with respect to the heating ramp used at 600ºC. This thesis reported nanostructure collapse at a heating rate of 1ºC/min, while previous studies have noted the same evidences at a rate of 2°C/min [58].

Appendix A

Autolab: Device Limitations

The Autolab device used in the EP optimization study can be set to a maximum potential range of 10V. When higher ranges are required, a transition between potentials occurs, which leads to the reboot of the software process. While switching potential ranges, the device takes some time to stabilize and continue the previous measures. Thus, the readings taken within this stabilization time range are not reliable. Figure A.1 shows the polarization curve from Figure 3.1 with the data recorded in the potential transition range. The sharp increase in current density in the 10-12V range is indicative of the stabilization period when switching potential ranges, and so it does not have any physical interpretation.

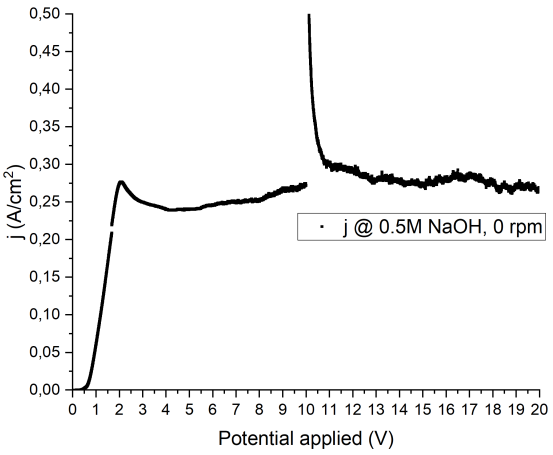

FIGURE A.1: Current density-voltage curve of W EP with aqueous electrolyte containing 0.5M NaOH without rotation speed.

Appendix B

XRD Characterization: Peak Deconvolution and Analysis

Peak deconvolution of all annealed samples characterised using X-Ray diffraction was achieved using the software *Origin*. From the XRD spectrum, the diffraction peaks of the WO_3 triplet were selected to perform *Multipeak Fit*. Peak fitting was performed with a Pseudo-Voigt function (equation B.1):

$$I = I_0 A m_u \left(\frac{2}{\pi} \frac{w}{4(\theta - \theta_c)^2 + w^2} + (1 - m_u) \frac{\sqrt{4ln(2)}}{\sqrt{\pi} w} e^{-\frac{4ln(2)}{w^2}(\theta - \theta_c)^2} \right) \tag{B.1}$$

where I_0 is the intensity offset, A is the area, m_u is the profile shape factor, θ_c is the peak centre and w is the full width at half maximum (FWHM).

Lattice parameters (a, b, c) were determined assuming $\beta = 90.89^o$ (JCPDS 01-083-0950). The spacing between diffraction peaks (d) of the monoclinic unit cell is defined in equation B.2:

$$\frac{1}{d^2} = \frac{1}{\sin^2 \beta} \left(\frac{h^2}{a^2} + k^2 \frac{\sin^2 \beta}{b^2} + \frac{l^2}{c^2} - \frac{2hl \cos \beta}{ac} \right) \tag{B.2}$$

where h, k, l are the Miller indices.

Bibliography

[1] G. A. Jones and K. J. Warner, "The 21st century population-energy-climate nexus," *Energy Policy*, vol. 93, pp. 206–212, 2016. [Online]. Available: https://www.sciencedirect.com/science/article/pii/S0301421516300830 [Cited on page 1.]

[2] S. F. Lincoln, "Fossil fuels in the 21st century," *Ambio*, vol. 34, no. 8, pp. 621–627, 2005. [Online]. Available: http://www.jstor.org/stable/4315666 [Cited on page 1.]

[3] R. Prăvălie, C. Patriche, and G. Bandoc, "Spatial assessment of solar energy potential at global scale. a geographical approach," *Journal of Cleaner Production*, vol. 209, pp. 692–721, 2019. [Online]. Available: https://www.sciencedirect.com/science/article/pii/S0959652618332657 [Cited on page 1.]

[4] M. B. Hayat, D. Ali, K. C. Monyake, L. Alagha, and N. Ahmed, "Solar energy—a look into power generation, challenges, and a solar-powered future," *International Journal of Energy Research*, vol. 43, no. 3, pp. 1049–1067, 2019. [Online]. Available: https://onlinelibrary.wiley.com/doi/abs/10.1002/er.4252 [Cited on page 1.]

[5] A. I. Osman, L. Chen, M. Yang, G. Msigwa, M. Farghali, S. Fawzy, D. W. Rooney, and P.-S. Yap, "Cost, environmental impact, and resilience of renewable energy under a changing climate: a review," *Environmental Chemistry Letters*, vol. 21, no. 2, pp. 741–764, 2023. [Online]. Available: https://doi.org/10.1007/s10311-022-01532-8 [Cited on page 1.]

[6] A. Bughneda, M. Salem, A. Richelli, D. Ishak, and S. Alatai, "Review of multilevel inverters for pv energy system applications," *Energies*, vol. 14, no. 6, 2021. [Online]. Available: https://www.mdpi.com/1996-1073/14/6/1585 [Cited on page 1.]

[7] C. Jiang, S. J. Moniz, A. Wang, T. Zhang, and J. Tang, "Photoelectrochemical devices for solar water splitting–materials and challenges," *Chemical Society Reviews*, vol. 46, no. 15, pp. 4645–4660, 2017. [Cited on pages 1, 3, and 4.]

[8] J. E. Trancik, "Renewable energy: Back the renewables boom," *Nature*, vol. 507, no. 7492, pp. 300–302, 2014. [Online]. Available: https://doi.org/10.1038/507300a [Cited on page 2.]

[9] L. Clarizia, M. N. Nadagouda, and D. D. Dionysiou, "Recent advances and challenges of photoelectrochemical cells for hydrogen production," *Current Opinion in Green and Sustainable Chemistry*, vol. 41, p. 100825, 2023. [Online]. Available: https://www.sciencedirect.com/science/article/pii/S2452223623000743 [Cited on pages 2 and 3.]

[10] Z. Wang, H. Zhu, W. Tu, X. Zhu, Y. Yao, Y. Zhou, and Z. Zou, "Host/guest nanostructured photoanodes integrated with targeted enhancement strategies for photoelectrochemical water splitting," *Advanced Science*, vol. 9, 11 2021. [Cited on pages xvii, 2, and 3.]

[11] R. Purchase, H. Vriend, H. Groot, P. Harmsen, and H. Bos, *Artificial photosynthesis for the conversion of sunlight to fuel*, 01 2015. [Cited on page 4.]

[12] M. B. Costa, M. A. de Araújo, M. V. de Lima Tinoco, J. F. de Brito, and L. H. Mascaro, "Current trending and beyond for solar-driven water splitting reaction on wo3 photoanodes," *Journal of Energy Chemistry*, vol. 73, pp. 88–113, 2022. [Online]. Available: https://www.sciencedirect.com/science/article/pii/S2095495622003102 [Cited on pages 4 and 7.]

[13] N. D. Sankir and M. Sankir, *Photoelectrochemical Solar Cells*. John Wiley & Sons, 2018. [Cited on page 4.]

[14] A. K. I. R. A. FUJISHIMA and K. E. N. I. C. H. I. HONDA, "Electrochemical photolysis of water at a semiconductor electrode," *Nature*, vol. 238, no. 5358, pp. 37–38, 1972. [Online]. Available: https://doi.org/10.1038/238037a0 [Cited on page 4.]

[15] S. Hejazi, M. Altomare, and P. Schmuki, "Photo-electrochemical solar-to-fuel energy conversion by hematite-based photo-anodes – the role of 1d nanostructuring," *Zeitschrift für Physikalische Chemie*, vol. 234, no. 4, pp. 615–631, 2020. [Online]. Available: https://doi.org/10.1515/zpch-2019-1479 [Cited on pages xvii and 5.]

[16] P. I. Kyesmen, N. Nombona, and M. Diale, "Influence of coating techniques on the optical and structural properties of hematite thin films," *Surfaces and Interfaces*, vol. 17, p. 100384, 2019. [Online]. Available: https://www.sciencedirect.com/science/article/pii/S2468023019303815 [Cited on page 4.]

[17] X. Luo, F. Li, B. Xu, Z. Sun, and L. Xu, "Enhanced photovoltaic response of the first polyoxometalate-modified zinc oxide photoanode for solar cell application," *J. Mater. Chem.*, vol. 22, pp. 15 050–15 055, 2012. [Online]. Available: http://dx.doi.org/10.1039/C2JM16018H [Cited on page 4.]

[18] G. A. R. Y. HODES, D. A. V. I. D. CAHEN, and J. O. O. S. T. MANASSEN, "Tungsten trioxide as a photoanode for a photoelectrochemical cell (pec)," *Nature*, vol. 260, no. 5549, pp. 312–313, 1976. [Online]. Available: https://doi.org/10.1038/260312a0 [Cited on page 4.]

[19] D. H. Kim, Y.-S. Shim, J.-M. Jeon, H. Y. Jeong, S. S. Park, Y.-W. Kim, J.-S. Kim, J.-H. Lee, and H. W. Jang, "Vertically ordered hematite nanotube array as an ultrasensitive and rapid response acetone sensor," *ACS Appl. Mater. Interfaces*, vol. 6, no. 17, pp. 14 779–14 784, Sep. 2014. [Online]. Available: https://doi.org/10.1021/am504156w [Cited on page 4.]

[20] A. G. Tamirat, J. Rick, A. A. Dubale, W.-N. Su, and B.-J. Hwang, "Using hematite for photoelectrochemical water splitting: a review of current progress and challenges," *Nanoscale Horiz.*, vol. 1, pp. 243–267, 2016. [Online]. Available: http://dx.doi.org/10.1039/C5NH00098J [Cited on page 4.]

[21] M. Butler, R. Nasby, and R. K. Quinn, "Tungsten trioxide as an electrode for photoelectrolysis of water," *Solid State Communications*, vol. 19, no. 10, pp. 1011–1014, 1976. [Online]. Available: https://www.sciencedirect.com/science/article/pii/0038109876906426 [Cited on page 5.]

[22] O. Samuel, M. H. D. Othman, R. Kamaludin, O. Sinsamphanh, H. Abdullah, M. H. Puteh, and T. A. Kurniawan, "Wo3–based photocatalysts: A review on synthesis, performance enhancement and photocatalytic memory for environmental applications," *Ceramics International*, vol. 48, no. 5, pp. 5845–5875, 2022. [Online]. Available: https://www.sciencedirect.com/science/article/pii/S0272884221035641 [Cited on page 5.]

[23] M. Zych, K. Syrek, M. Pisarek, and G. D. Sulka, "Anodic wo3 layers sensitized with hematite operating under the visible light spectrum," *Journal of Power Sources*, vol. 541, p. 231656, 2022. [Online]. Available: https://www.sciencedirect.com/science/article/pii/S0378775322006553 [Cited on page 5.]

[24] Y. Shabdan, A. Markhabayeva, N. Bakranov, and N. Nuraje, "Photoactive tungsten-oxide nanomaterials for water-splitting," *Nanomaterials*, vol. 10, no. 9, 2020. [Online]. Available: https://www.mdpi.com/2079-4991/10/9/1871 [Cited on page 5.]

[25] G. Zheng, J. Wang, H. Liu, V. Murugadoss, G. Zu, H. Che, C. Lai, H. Li, T. Ding, Q. Gao *et al.*, "Tungsten oxide nanostructures and nanocomposites for photoelectrochemical water splitting," *Nanoscale*, vol. 11, no. 41, pp. 18 968–18 994, 2019. [Cited on pages 5, 7, and 10.]

[26] X. Liu, F. Wang, and Q. Wang, "Nanostructure-based wo3 photoanodes for photoelectrochemical water splitting," *Phys. Chem. Chem. Phys.*, vol. 14, pp. 7894–7911, 2012. [Online]. Available: http://dx.doi.org/10.1039/C2CP40976C [Cited on pages 5 and 6.]

[27] S. Wang, W. Fan, Z. Liu, A. Yu, and X. Jiang, "Advances on tungsten oxide based photochromic materials: strategies to improve their photochromic properties," *Journal of Materials Chemistry C*, vol. 6, no. 2, pp. 191–212, 2018. [Cited on pages xvii, 5, 6, 7, and 8.]

[28] J. Huang, P. Yue, L. Wang, H. She, and Q. Wang, "A review on tungsten-trioxide-based photoanodes for water oxidation," *Chinese Journal of Catalysis*, vol. 40, no. 10, pp. 1408–1420, 2019. [Online]. Available: https://www.sciencedirect.com/science/article/pii/S1872206719633991 [Cited on pages 6 and 10.]

[29] B. Gerand, G. Nowogrocki, J. Guenot, and M. Figlarz, "Structural study of a new hexagonal form of tungsten trioxide," *Journal of Solid State Chemistry*, vol. 29, no. 3, pp. 429–434, 1979. [Online]. Available: https://www.sciencedirect.com/science/article/pii/0022459679901993 [Cited on page 6.]

[30] M. Yang, N. K. Shrestha, and P. Schmuki, "Thick porous tungsten trioxide films by anodization of tungsten in fluoride containing phosphoric acid electrolyte," *Electrochemistry Communications*, vol. 11, no. 10, pp. 1908–1911,

2009. [Online]. Available: https://www.sciencedirect.com/science/article/pii/S1388248109003865 [Cited on page 6.]

[31] M. Weil and W.-D. Schubert, "The beautiful colours of tungsten oxides," 2013. [Online]. Available: https://api.semanticscholar.org/CorpusID:31645217 [Cited on pages xvii and 7.]

[32] H. M. Chen, C. K. Chen, R.-S. Liu, L. Zhang, J. Zhang, and D. P. Wilkinson, "Nano-architecture and material designs for water splitting photoelectrodes," *Chemical Society Reviews*, vol. 41, no. 17, pp. 5654–5671, 2012. [Cited on pages 7 and 25.]

[33] Y. Kuang, Q. Jia, H. Nishiyama, T. Yamada, A. Kudo, and K. Domen, "A front-illuminated nanostructured transparent bivo4 photoanode for¿ 2% efficient water splitting," *Advanced Energy Materials*, vol. 6, no. 2, p. 1501645, 2016. [Cited on page 7.]

[34] Y. Yu, Z. Zhang, X. Yin, A. Kvit, Q. Liao, Z. Kang, X. Yan, Y. Zhang, and X. Wang, "Enhanced photoelectrochemical efficiency and stability using a conformal tio2 film on a black silicon photoanode," *Nature Energy*, vol. 2, no. 6, pp. 1–7, 2017. [Cited on page 7.]

[35] S. Emin, M. De Respinis, M. Fanetti, W. Smith, M. Valant, and B. Dam, "A simple route for preparation of textured wo3 thin films from colloidal w nanoparticles and their photoelectrochemical water splitting properties," *Applied Catalysis B: Environmental*, vol. 166, pp. 406–412, 2015. [Cited on page 7.]

[36] J. Su, X. Feng, J. D. Sloppy, L. Guo, and C. A. Grimes, "Vertically aligned wo3 nanowire arrays grown directly on transparent conducting oxide coated glass: synthesis and photoelectrochemical properties," *Nano letters*, vol. 11, no. 1, pp. 203–208, 2011. [Cited on page 7.]

[37] S. S. Kalanur, Y. J. Hwang, S. Y. Chae, and O. S. Joo, "Facile growth of aligned wo 3 nanorods on fto substrate for enhanced photoanodic water oxidation activity," *Journal of Materials Chemistry A*, vol. 1, no. 10, pp. 3479–3488, 2013. [Cited on page 7.]

[38] S. Shin, H. S. Han, J. S. Kim, I. J. Park, M. H. Lee, K. S. Hong, and I. S. Cho, "A tree-like nanoporous wo 3 photoanode with enhanced charge transport efficiency for photoelectrochemical water oxidation," *Journal of Materials Chemistry A*, vol. 3, no. 24, pp. 12 920–12 926, 2015. [Cited on page 7.]

[39] M. M. Abouelela, G. Kawamura, W. K. Tan, and A. Matsuda, "Anodic nanoporous wo3 modified with bi2s3 quantum dots as a photoanode for photoelectrochemical water splitting," *Journal of Colloid and Interface Science*, vol. 629, pp. 958–970, 2023. [Cited on page 7.]

[40] R. do Nascimento Simões, "Mastering anodic nanostructured wo3 for solar water splitting," 2022. [Cited on pages xvii, 8, 9, 10, 20, 21, 22, 24, 26, 42, 44, 48, 50, 51, 53, 54, 57, and 60.]

[41] A. Apolinário, C. T. Sousa, G. N. P. Oliveira, A. M. L. Lopes, J. Ventura, L. Andrade, A. Mendes, and J. P. Araújo, "Tailoring the anodic hafnium oxide morphology using different organic solvent electrolytes," *Nanomaterials*, vol. 10, no. 2, 2020. [Online]. Available: https://www.mdpi.com/2079-4991/10/2/382 [Cited on page 8.]

[42] D. Rodríguez and P. Perillo, "Ultra-fast tio2 nanopores broadband photodetector," *Optical Materials*, vol. 135, p. 113315, 2023. [Online]. Available: https://www.sciencedirect.com/science/article/pii/S0925346722013544

[43] S. S. Thind, M. Paul, J. Hayden, A. Joshi, D. Goodlett, and J. S. McIndoe, "A highly efficient photocatalytic system for environmental applications based on tio2 nanomaterials," *Industrial Chemistry & Materials*, 2023. [Cited on page 8.]

[44] N. Cabrera and N. F. Mott, "Theory of the oxidation of metals," *Reports on progress in physics*, vol. 12, no. 1, p. 163, 1949. [Cited on page 8.]

[45] A. Apolinário, P. Quitério, C. T. Sousa, J. Ventura, J. B. Sousa, L. Andrade, A. M. Mendes, and J. P. Araújo, "Modeling the growth kinetics of anodic tio2 nanotubes," *J. Phys. Chem. Lett.*, vol. 6, no. 5, pp. 845–851, Mar. 2015. [Online]. Available: https://doi.org/10.1021/jz502380b [Cited on page 8.]

[46] Y.-C. Nah, A. Ghicov, D. Kim, and P. Schmuki, "Enhanced electrochromic properties of self-organized nanoporous wo3," *Electrochemistry Communications*, vol. 10, no. 11, pp. 1777–1780, 2008. [Cited on page 9.]

[47] A. Apolinário, C. Sousa, J. Ventura, J. Costa, D. Leitao, J. Moreira, J. Sousa, L. Andrade, A. Mendes, and J. Araújo, "The role of the ti surface roughness in the self-ordering of tio 2 nanotubes: a detailed study of the growth mechanism," *Journal of Materials Chemistry A*, vol. 2, no. 24, pp. 9067–9078, 2014. [Cited on page 9.]

[48] F. Li, L. Zhang, and R. M. Metzger, "On the growth of highly ordered pores in anodized aluminum oxide," *Chemistry of materials*, vol. 10, no. 9, pp. 2470–2480, 1998. [Cited on page 10.]

[49] N. Mukherjee, M. Paulose, O. K. Varghese, G. K. Mor, and C. A. Grimes, "Fabrication of nanoporous tungsten oxide by galvanostatic anodization," *Journal of Materials Research*, vol. 18, no. 10, pp. 2296–2299, 2003. [Online]. Available: https://doi.org/10.1557/JMR.2003.0321 [Cited on page 10.]

[50] A. S. Martins, T. T. Guaraldo, J. Wenk, D. Mattia, and M. V. Boldrin Zanoni, "Nanoporous wo3 grown on a 3d tungsten mesh by electrochemical anodization for enhanced photoelectrocatalytic degradation of tetracycline in a continuous flow reactor," *Journal of Electroanalytical Chemistry*, vol. 920, p. 116617, 2022. [Online]. Available: https://www.sciencedirect.com/science/article/pii/S1572665722006099 [Cited on page 10.]

[51] A. M. Mohamed, S. A. Shaban, H. A. El Sayed, B. E. Alanadouli, and N. K. Allam, "Morphology–photoactivity relationship: Wo3 nanostructured films for solar hydrogen production," *International Journal of Hydrogen Energy*, vol. 41, no. 2, pp. 866–872, 2016. [Online]. Available: https://www.sciencedirect.com/science/article/pii/S0360319915303724 [Cited on pages 10 and 57.]

[52] R. Hahn, J. Macak, and P. Schmuki, "Rapid anodic growth of tio2 and wo3 nanotubes in fluoride free electrolytes," *Electrochemistry Communications*, vol. 9, no. 5, pp. 947–952, 2007. [Online]. Available: https://www.sciencedirect.com/science/article/pii/S1388248106005613 [Cited on page 10.]

[53] K. Syrek, L. Zaraska, M. Zych, and G. D. Sulka, "The effect of anodization conditions on the morphology of porous tungsten oxide layers formed in aqueous solution," *Journal of Electroanalytical Chemistry*, vol. 829, pp. 106–115, 2018. [Online]. Available: https://www.sciencedirect.com/science/article/pii/S1572665718306556 [Cited on page 10.]

[54] M. Zych, K. Syrek, L. Zaraska, and G. D. Sulka, "Improving photoelectrochemical properties of anodic wo3 layers by optimizing electrosynthesis conditions," *Molecules*, vol. 25, no. 12, 2020. [Online]. Available: https://www.mdpi.com/1420-3049/25/12/2916 [Cited on pages 10 and 60.]

[55] L. Li, X. Zhao, D. Pan, and G. Li, "Nanotube array-like wo3/w photoanode fabricated by electrochemical anodization for photoelectrocatalytic overall water splitting," *Chinese Journal of Catalysis*, vol. 38, no. 12, pp. 2132–2140, 2017. [Cited on page 10.]

[56] D. Rana, "Fabrication and characterization of low dimensional metal oxides and sulfides for solar energy conversion," 2023. [Cited on page 10.]

[57] C. Y. Ng, K. Abdul Razak, and Z. Lockman, "Effect of annealing temperature on anodized nanoporous wo3," *Journal of Porous Materials*, vol. 22, no. 2, pp. 537–544, 2015. [Online]. Available: https://doi.org/10.1007/s10934-015-9924-x [Cited on pages 10, 11, and 54.]

[58] K. Syrek, M. Zych, L. Zaraska, and G. D. Sulka, "Influence of annealing conditions on anodic tungsten oxide layers and their photoelectrochemical activity," *Electrochimica Acta*, vol. 231, pp. 61–68, 2017. [Online]. Available: https://www.sciencedirect.com/science/article/pii/S0013468617303031 [Cited on pages 11, 22, 53, 54, and 65.]

[59] A. M. Mohamed, S. A. Shaban, H. A. El Sayed, B. E. Alanadouli, and N. K. Allam, "Morphology-photoactivity relationship: Wo3 nanostructured films for solar hydrogen production," *International Journal of Hydrogen Energy*, vol. 41, no. 2, pp. 866–872, 2016. [Online]. Available: https://www.sciencedirect.com/science/article/pii/S0360319915303724 [Cited on page 11.]

[60] K. soon Ahn, S. Lee, A. C. Dillon, C. E. Tracy, and R. J. Pitts, "The effect of thermal annealing on photoelectrochemical responses of wo3 thin films," *Journal of Applied Physics*, vol. 101, p. 093524, 2007. [Online]. Available: https://api.semanticscholar.org/CorpusID:122726110 [Cited on page 11.]

[61] W. Han and F. Fang, "Fundamental aspects and recent developments in electropolishing," *International Journal of Machine Tools and Manufacture*, vol. 139, pp. 1–23, 2019. [Online]. Available: https://www.sciencedirect.com/science/article/pii/S0890695518301925 [Cited on pages xvii, 12, 13, 14, 16, 18, 30, and 31.]

[62] D. Landolt, "Fundamental aspects of electropolishing," *Electrochimica Acta*, vol. 32, no. 1, pp. 1–11, 1987. [Online]. Available: https://www.sciencedirect.com/science/article/pii/0013468687870019 [Cited on pages 11, 13, and 16.]

[63] G. Wynick and C. Boehlert, "Use of electropolishing for enhanced metallic specimen preparation for electron backscatter diffraction analysis," *Materials Characterization*, vol. 55, no. 3, pp. 190–202, 2005. [Online]. Available: https://www.sciencedirect.com/science/article/pii/S1044580305001099 [Cited on page 12.]

[64] J. A. McGeough, *Principles of electrochemical machining*. Chapman and Hall and Halsted Press Division, Wiley, 1974. [Online]. Available: https://cir.nii.ac.jp/crid/1130000797072855040 [Cited on page 12.]

[65] T.-R. Lin and C.-R. Su, "Experimental study of lapping and electropolishing of tungsten carbides," *The International Journal of Advanced Manufacturing Technology*, vol. 36, no. 7, pp. 715–723, 2008. [Online]. Available: https://doi.org/10.1007/s00170-006-0895-6 [Cited on page 12.]

[66] P. A. Jacquet, "Electrolytic and chemical polishing," *Metallurgical Reviews*, vol. 1, no. 1, pp. 157–238, 1956. [Online]. Available: https://doi.org/10.1179/mtlr.1956.1.1.157 [Cited on pages 12 and 13.]

[67] G. Yang, B. Wang, K. Tawfiq, H. Wei, S. Zhou, and G. Chen, "Electropolishing of surfaces: theory and applications," *Surface Engineering*, vol. 33, no. 2, pp. 149–166, 2017. [Online]. Available: https://doi.org/10.1080/02670844.2016.1198452 [Cited on pages xvii, 13, 14, 16, 18, and 30.]

[68] S. Jin, X. lu, L. Lin, and K. Zhao, "Study of buffered electropolishing on niobium sheet," 08 2023. [Cited on pages 12, 17, and 18.]

[69] M. Matlosz, S. Magaino, and D. Landolt, "Impedance analysis of a model mechanism for acceptor-limited electropolishing," *Journal of The Electrochemical Society*, vol. 141, no. 2, p. 410, feb 1994. [Online]. Available: https://dx.doi.org/10.1149/1.2054741 [Cited on page 13.]

[70] S. Magaino, M. Matlosz, and D. Landolt, "An impedance study of stainless steel electropolishing," *Journal of The Electrochemical Society*, vol. 140, no. 5, p. 1365, may 1993. [Online]. Available: https://dx.doi.org/10.1149/1.2221562 [Cited on pages 13 and 18.]

[71] C. Wagner, "Contribution to the theory of electropolishing," *Journal of The Electrochemical Society*, vol. 101, no. 5, p. 225, may 1954. [Online]. Available: https://dx.doi.org/10.1149/1.2781235 [Cited on page 14.]

[72] W. Han and F.-Z. Fang, "Investigation of electropolishing characteristics of tungsten in eco-friendly sodium hydroxide aqueous solution," *Advances in Manufacturing*, vol. 8, no. 3, pp. 265–278, 2020. [Online]. Available: https://doi.org/10.1007/s40436-020-00309-y [Cited on pages xvii, 14, 16, 17, 18, 29, 30, and 35.]

[73] J. Edwards, "The mechanism of electropolishing of copper in phosphoric acid solutions: Ii . the mechanism of smoothing," *Journal of The Electrochemical Society*, vol. 100, no. 8, p. 223C, aug 1953. [Online]. Available: https://dx.doi.org/10.1149/1.2781129 [Cited on page 14.]

[74] F. Wang, X. Zhang, and H. Deng, "A comprehensive study on electrochemical polishing of tungsten," *Applied Surface Science*, vol. 475, pp. 587–597, 2019. [Online]. Available: https://www.sciencedirect.com/science/article/pii/S0169433219300297 [Cited on pages 14, 15, 18, 29, and 34.]

[75] W. C. Elmore, "Electrolytic Polishing," *Journal of Applied Physics*, vol. 10, no. 10, pp. 724–727, 04 2004. [Online]. Available: https://doi.org/10.1063/1.1707257 [Cited on page 14.]

[76] H. O. A. R. T. P. and J. A. S. MOWAT, "Mechanism of electropolishing," *Nature*, vol. 165, no. 4185, pp. 64–65, 1950. [Online]. Available: https://doi.org/10.1038/165064a0 [Cited on page 14.]

[77] R. D. Grimm, A. C. West, and D. Landolt, "Ac impedance study of anodically formed salt films on iron in chloride solution," *Journal of The Electrochemical Society*, vol. 139, no. 6, p. 1622, jun 1992. [Online]. Available: https://dx.doi.org/10.1149/1.2069467 [Cited on page 14.]

[78] R. Yi, J. Ji, Z. Zhan, and H. Deng, "Mechanism study of electropolishing from the perspective of etching isotropy," *Journal of Materials Processing Technology*, vol. 305, p. 117599, 2022. [Online]. Available: https://www.sciencedirect.com/science/article/pii/S092401362200111X [Cited on pages xvii, 15, 16, 17, 18, 29, 30, and 34.]

[79] D. Ma, S. Li, and C. Liang, "Electropolishing of high-purity aluminium in perchloric acid and ethanol solutions," *Corrosion Science*, vol. 51, no. 4, pp. 713–718, 2009. [Online]. Available: https://www.sciencedirect.com/science/article/pii/S0010938X09000328 [Cited on page 16.]

[80] W. Krauss, N. Holstein, and J. Konys, "Strategies in electro-chemical machining of tungsten for divertor application," *Fusion Engineering and Design*, vol. 82, no. 15, pp. 1799–1805, 2007, proceedings of the 24th Symposium on Fusion Technology. [Online]. Available: https://www.sciencedirect.com/science/article/pii/S0920379607003328 [Cited on pages 17 and 21.]

[81] K. Fushimi, M. Stratmann, and A. W. Hassel, "Electropolishing of niti shape memory alloys in methanolic h2so4," *Electrochimica Acta*, vol. 52, no. 3, pp. 1290–1295, 2006. [Online]. Available: https://www.sciencedirect.com/science/article/pii/S001346860600764X [Cited on page 17.]

[82] P. S. Pa and H. Hocheng, "Continuous secondary ultrasonic electropolishing of an skd61 cylindrical part," *The International Journal of Advanced Manufacturing Technology*, vol. 21, no. 4, pp. 238–242, 2003. [Online]. Available: https://doi.org/10.1007/s001700300027 [Cited on page 17.]

[83] M. Haïdopoulos, S. Turgeon, C. Sarra-Bournet, G. Laroche, and D. Mantovani, "Development of an optimized electrochemical process for subsequent coating of 316 stainless steel for stent applications," *Journal of Materials Science: Materials in Medicine*, vol. 17, no. 7, pp. 647–657, 2006. [Online]. Available: https://doi.org/10.1007/s10856-006-9228-4 [Cited on page 17.]

[84] E. S. Lee and T. H. Shin, "An evaluation of the machinability of nitinol shape memory alloy by electrochemical polishing," *Journal of Mechanical Science and Technology*, vol. 25, no. 4, pp. 963–969, 2011. [Online]. Available: https://doi.org/10.1007/s12206-011-0209-2

[85] F. Nazneen, P. Galvin, D. W. M. Arrigan, M. Thompson, P. Benvenuto, and G. Herzog, "Electropolishing of medical-grade stainless steel in preparation for surface nano-texturing," *Journal of Solid State Electrochemistry*, vol. 16, no. 4, pp. 1389–1397, 2012. [Online]. Available: https://doi.org/10.1007/s10008-011-1539-9 [Cited on page 17.]

[86] A. Chandra, M. Sumption, and G. S. Frankel, "On the mechanism of niobium electropolishing," *Journal of The Electrochemical Society*, vol. 159, no. 11, p. C485, sep 2012. [Online]. Available: https://dx.doi.org/10.1149/2.054211jes [Cited on page 18.]

[87] A. Apolinario, T. Lopes, C. Costa, J. P. Araujo, and A. M. Mendes, "Multilayered wo3 nanoplatelets for efficient photoelectrochemical water splitting: the role of the annealing ramp," *ACS Applied Energy Materials*, vol. 2, no. 2, pp. 1040–1050, 2019. [Cited on page 22.]

[88] S. M. Salapaka, A. Ramamoorthy, and M. V. Salapaka, "Afm imaging?reliable or not?: Validation and verification of images in atomic force microscopy," *IEEE Control Systems*, vol. 33, pp. 106–118, 2013. [Online]. Available: https://api.semanticscholar.org/CorpusID:8909691 [Cited on page 22.]

[89] A. O. A. d. S. Apolinario, "Nanostructured photoanodes for solar cells," *Ph. D. Thesis*, 2015. [Cited on page 22.]

[90] N. Mourougou-Candoni, "Tapping mode afm imaging for functionalized surfaces," 2012. [Online]. Available: https://api.semanticscholar.org/CorpusID:137385330 [Cited on page 22.]

[91] W. Zhou and Z. L. Wang, *Scanning microscopy for nanotechnology: techniques and applications*. Springer science & business media, 2007. [Cited on pages 23 and 24.]

[92] B. J. Inkson, G. Hübschen, I. Altpeter, R. Tschuncky, and H.-G. Herrmann, "2 - scanning electron microscopy (sem) and transmission electron microscopy (tem) for materials characterization," in *Materials Characterization Using Nondestructive Evaluation (NDE) Methods*. Woodhead Publishing, 2016, pp. 17–43. [Online]. Available: https://www.sciencedirect.com/science/article/pii/B978008100040300002X [Cited on pages xvii, 23, and 24.]

[93] M. Abd Mutalib, M. A. Rahman, M. H. D. Othman, A. F. Ismail, J. Jaafar, N. Hilal, A. F. Ismail, T. Matsuura, and D. Oatley-Radcliffe, "Chapter 9 - scanning electron microscopy (sem) and energy-dispersive x-ray (edx) spectroscopy," in *Membrane Characterization*. Elsevier, 2017, pp. 161–179. [Online]. Available: https://www.sciencedirect.com/science/article/pii/B9780444637765000097 [Cited on page 24.]

[94] P. V. B. Quitério, "Environmentally friendly photoanodes for solar water splitting," 2020. [Cited on pages xvii, 24, 26, 27, and 48.]

[95] V. K. Pecharsky and P. Y. Zavalij, *Fundamentals of diffraction*. Springer, 2003. [Cited on page 24.]

[96] T. E. o. E. Britannica, *Bragg law*. Encyclopedia Britannica, 2022. [Cited on pages xvii and 25.]

[97] J. Y. Kim, G. Magesh, D. H. Youn, J.-W. Jang, J. Kubota, K. Domen, and J. S. Lee, "Single-crystalline, wormlike hematite photoanodes for efficient solar water splitting," *Scientific Reports*, vol. 3, no. 1, p. 2681, 2013. [Online]. Available: https://doi.org/10.1038/srep02681 [Cited on page 25.]

[98] X. Shi, L. Cai, M. Ma, X. Zheng, and J. H. Park, "General characterization methods for photoelectrochemical cells for solar water splitting," *ChemSusChem*, vol. 8, no. 19, pp. 3192–3203, 2015. [Cited on page 26.]

[99] H. Ramasawmy and L. Blunt, "Investigation of the effect of electrochemical polishing on edm surfaces," *The International Journal of Advanced Manufacturing Technology*, vol. 31, no. 11, pp. 1135–1147, 2007. [Online]. Available: https://doi.org/10.1007/s00170-005-0302-8 [Cited on page 32.]

[100] E.-S. Lee, "Machining characteristics of the electropolishing of stainless steel (sts316l)," *The International Journal of Advanced Manufacturing Technology*, vol. 16, no. 8, pp. 591–599, 2000. [Online]. Available: https://doi.org/10.1007/s001700070049 [Cited on page 32.]

[101] T. Masuzawa, "State of the art of micromachining," *CIRP Annals*, vol. 49, no. 2, pp. 473–488, 2000. [Online]. Available: https://www.sciencedirect.com/science/article/pii/S0007850607634519 [Cited on page 35.]

[102] S. Singh, W. R. Barden, and P. Kruse, "Nanopatterning of transition metal surfaces via electrochemical dimple array formation," *ACS nano*, vol. 2, no. 12, pp. 2453–2464, 2008. [Cited on pages 35 and 50.]

[103] J. R. Smith, S. Breakspear, and S. A. Campbell, "Afm in surface finishing: Part ii. surface roughness," *Transactions of the IMF*, vol. 81, no. 3, pp. B55–B58, 2003. [Cited on page 36.]

[104] C. W. Lai, S. B. Abd Hamid, S. Sreekantan *et al.*, "A novel solar driven photocatalyst: well-aligned anodic wo 3 nanotubes," *International Journal of Photoenergy*, vol. 2013, 2013. [Cited on page 42.]

[105] K. Kalantar-zadeh, A. Z. Sadek, H. Zheng, V. Bansal, S. K. Bhargava, W. Wlodarski, J. Zhu, L. Yu, and Z. Hu, "Nanostructured wo3 films using high temperature anodization," *Sensors and Actuators B: Chemical*, vol. 142, no. 1, pp. 230–235, 2009. [Cited on page 42.]

[106] A. Apolinário, C. Sousa, J. Ventura, L. Andrade, A. Mendes, and J. Araújo, "Tailoring the ti surface via electropolishing nanopatterning as a route to obtain highly ordered tio2 nanotubes," *Nanotechnology*, vol. 25, no. 48, p. 485301, 2014. [Cited on pages 42 and 44.]

[107] P. Li, H. Wang, Y. Ni, Y. Song, M. Sun, T. Gong, C. Li, and X. Zhu, "Unraveling the six stages of the current–time curve and the bilayer nanotubes obtained by one-step anodization of zr," *Nanoscale Advances*, vol. 4, no. 2, pp. 582–589, 2022. [Cited on page 42.]

[108] K. Nielsch, J. Choi, K. Schwirn, R. B. Wehrspohn, and U. Gösele, "Self-ordering regimes of porous alumina: the 10 porosity rule," *Nano letters*, vol. 2, no. 7, pp. 677–680, 2002. [Cited on page 47.]

[109] J. W. Diggle, T. C. Downie, and C. W. Goulding, "Anodic oxide films on aluminum," *Chem. Rev.*, vol. 69, no. 3, pp. 365–405, Jun. 1969. [Online]. Available: https://doi.org/10.1021/cr60259a005 [Cited on page 49.]

[110] Q. Zhou, M. Tian, Z. Ying, Y. Dan, F. Tang, J. Zhang, J. Zhu, and X. Zhu, "Dense films formed during ti anodization in nh4f electrolyte: Evidence against the field-assisted dissolution reactions of fluoride ions," *Electrochemistry Communications*, vol. 111, p. 106663, 2020. [Online]. Available: https://www.sciencedirect.com/science/article/pii/S138824812030014X [Cited on page 49.]

[111] D. Leitao, A. Apolinario, C. Sousa, J. Ventura, J. Sousa, M. Vazquez, and J. Araujo, "Nanoscale topography: a tool to enhance pore order and pore size distribution in anodic aluminum oxide," *The Journal of Physical Chemistry C*, vol. 115, no. 17, pp. 8567–8572, 2011. [Cited on page 50.]

[112] S. Wang, H. Chen, G. Gao, T. Butburee, M. Lyu, S. Thaweesak, J.-H. Yun, A. Du, G. Liu, and L. Wang, "Synergistic crystal facet engineering and structural control of wo3 films exhibiting unprecedented photoelectrochemical performance," *Nano*

Energy, vol. 24, pp. 94–102, 2016. [Online]. Available: https://www.sciencedirect.com/science/article/pii/S221128551630057X [Cited on page 57.]